

Design principles for a single-process 3D-printed stacked dielectric actuators – theory and experiment

Tibor Barši Palmič^a, Janko Slavič^{a,*}

^a*University of Ljubljana, Faculty of Mechanical Engineering, Aškerčeva 6, 1000 Ljubljana, Slovenia*

Cite as:

Tibor Barši Palmič and Janko Slavič, Design principles for a single-process 3D-printed stacked dielectric actuators – theory and experiment, International Journal of Mechanical Sciences (2023), <https://doi.org/10.1016/j.ijmecsci.2023.108128>

Abstract

Fully 3D-printed smart structures have attracted a lot of research interest; new technologies, materials, and methods for 3D-printed functional structures such as sensors, actuators, generators, and batteries are being researched. Recently, a fully 3D-printed, dynamic dielectric actuator fabricated in a single process with multi-material thermoplastic filament extrusion was presented. However, the effects of design parameters on the dynamic electromechanical properties of the printed actuator were not yet researched.

To achieve the required performance and dynamic properties of an individualised, 3D-printed actuator, the electromechanical properties must be related to the theoretical design parameters. This requires research into the properties of 3D-printed materials and the electromechanical modelling of the 3D-printed actuator.

In this research, an analytical, electromechanical model is introduced, consisting of electrical and mechanical models, and electromechanical coupling. The model consists of basic electrical and dynamic lumped elements, which facilitates the reproducibility and extensibility of the model. The electrical and electromechanical model have been experimentally validated in a free-displacement and a blocked-force boundary condition.

*Corresponding author

Email address: janko.slavic@fs.uni-lj.si (Janko Slavič)

This research leads to the identification of design principles and the ability to customize and adapt the 3D-printed actuators to specific dynamic applications.

Keywords: smart structures, multi-material 3D printing, single process, 3D-printed actuator, stacked dielectric actuator, electromechanical model, free displacement, blocked force, design parameters

PACS: 0000, 1111

2000 MSC: 0000, 1111

1. Introduction

Smart structures are characterised by the ability to sense and respond to external stimuli. This requires the combination of several functions such as sensing and actuation, to be combined into a single structure [1, 2]. Multi-material additive manufacturing makes possible the production of customized devices in a single manufacturing process without the need for conventional or manual manufacturing interventions [3, 4].

Fully 3D-printed dynamic sensors [5] introduced in recent years are capable of measuring acceleration [6, 7], force [8, 9], pressure [10, 11], and strain [12, 13]. Conductive polymer nanocomposites enable the imprinting of conductive networks [14, 15] and passive electrical elements [16]. Polymers and polymer composites are being developed for the 3D printing of functional batteries [17, 18] and generators [19].

Dynamic solid-state actuators introduced in recent years enable a variety of devices with diverse capabilities. Some actuation mechanisms, such as electrostatic [20, 21], piezoelectric [22, 23], electromagnetic [24], and dielectric [25], are known for their fast response times and have been used in the creation of microbeam [26] and membrane [27] resonators, membrane speakers [28], and fast-switching bistable actuators [29]. Other actuation mechanisms, such as pneumatic [30], thermomechanical [31, 32], phase-change [33], and shape-memory [34], have slower response times and have been employed in the development of biomimetic robots [35], soft grippers [36], artificial muscles [37], and self-folding structures [38].

Additive manufacturing has become an important method for creating solid-state actuators due to its benefits, including low-cost single-process fabrication, customization, the ability to create complex shapes, fast prototyping, and integrated sensing [1].

Recently presented 3D-printed actuators are based on various physical mechanisms such as electromagnetic [39, 40], dielectric [41, 42], piezoelectric [43], and shape-memory effects [44, 45]. Recently, a fully 3D-printed, stacked dielectric actuator printed in a single process using commercial thermoplastic filament-extrusion technology and commercial filament materials was presented [41].

The solid-state design and flexible materials allow various configurations of the dielectric actuators, *e.g.*, stacked [41, 46] and bending actuators [47, 48], dielectric membranes [28], pre-stressed annular [49], balloon [25], and rolled cylindrical actuators [50], actuators with liquid electrodes [51] or liquid dielectric [52], and dielectric minimum-energy structures (DEMES) [53, 54]. The extensive configurations show applicability in various fields, *e.g.*, robots with dielectric muscles [55] that are able to walk [56], swim [57], jump [58, 59] and fly [60], applications in medicine, such as active lenses [61], tremor control [62], prosthetic [63], and soft haptic feedback devices [64], low-power dielectric grippers [54], micro- and nanopositioning systems [65], and vibro-acoustics, such as resonators [26, 27], loudspeakers [28], and vibro-isolation [27, 66].

To achieve the dynamic properties required for a particular application, the design principles must be understood. For this reason, the relationship between the design parameters and the dynamic properties must be studied.

In this manuscript, the design principles of a 3D-printed, dynamic, stacked dielectric actuator are investigated. A stacked dielectric actuator consists of dielectric and conductive layers stacked on top of each other to form a stack. The conductive layers are electrically connected to each other so that the electric field can be generated in each dielectric layer. When a voltage is applied, the actuator contracts in the direction perpendicular to the stacked layers.

Dielectric actuators require models that incorporate the electrical properties of the electrodes and dielectric, the electromechanical coupling, and the mechanical model of the materials that deform with the actuator [67]. Henann et al. presented the thermodynamic development of the three-dimensional, fully coupled theory and implemented the theory in commercial finite-element code Abaqus [68]. Sharma et al. addressed the anisotropic properties of dielectric elastomers and developed a nonlinear finite-element framework for anisotropic dielectric elastomers [69]. Jia et al. developed a linear control for a positioning dielectric system with multiple electrodes, which was achieved with the developed finite-element model, enabling lin-

earization of the relationship between the position of the control handle and the generated displacement [70]. In addition, a coupled electromechanical finite-element method (FEM) was used to study the electromechanical instability and the effect of pre-strain in soft dielectrics [71], wave propagation [72, 73], tunable wave-band gaps [74], and even the effect of humidity on the electromechanical properties [75].

The main drawback of models based on the FEM is the computational requirement. To obtain a faster and less computationally intensive model, the field equations can be formulated for a particular actuator configuration and boundary condition to obtain an analytical model that can be used to derive design principles and optimize the actuator. Wang et al. developed an analytical electromechanical model for a spring-connected conical DEA [49]. Karner et al. investigated how different viscoelastic constitutive models capture the time-dependent deformation of DEA under sinusoidal excitation [76]. Analytical models have also been developed to study the effect of mechanical pre-stress on the dynamic performance and stability of dielectric beams [77] and membranes [78].

The first studies on the design principles of classical stacked dielectric actuators were carried out by Kovacs et al. [79]. Manually fabricated stacks were loaded with a weight and excited with a static voltage to cause contraction. Kovacs et al. investigated the effects of the number of stacked layers, the width of the uncoated edge region (necessary to avoid electrical breakdown at the edge), and the effects of the stiff mechanical end adapters. Similarly, Kuhring et al. [80] investigated the effect of the number of layers, the ratio of active to total layer area, and the influence of a stiff mechanical connection.

Haus et al. [81] developed an analytical electromechanical model divided into a comprehensive electrical model and a mechanical model for static and dynamic operation. The model was parameterized by the experimental mechanical characterization of the fabricated stacked actuators [81]. Hoffstadt and Maas [82] developed an analytical electromechanical model to optimise the electromechanical conversion of the stacked transducer. The model was experimentally validated with silicone, polyurethane and natural rubber.

In this paper, we present a dynamic electromechanical model for fully 3D-printed stacked dielectric actuators. This type of actuator is made up of layers of active dielectric material, electrodes, and passive insulation, all of which are included in the model. The model consists of standard electrical elements (such as resistors and capacitors) and mechanical elements (such

as springs and masses) defined by material properties such as conductivity, permittivity, and elastic modulus. We present two formulations of the model, one for free-displacement and one for blocked-force operation, and validate the model using experimental data from nine actuators of different dimensions under different boundary conditions. This research is based on a previously presented paper about 3D-printing stacked dielectric actuators[41], and the developed model enables the optimization of design parameters for specific dynamic applications. The results of this work provide design principles that can be used to accurately predict the dynamic electromechanical properties of 3D-printed stacked dielectric actuators and optimize their design parameters, potentially reducing the development time of active dynamic structures through fewer design and manufacturing iterations.

The manuscript is organized as follows. In Sec. 2, the theoretical background and prior research are presented. In Sec. 3, the model consisting of the electrical and mechanical domains is introduced. The model is followed by the experimental methods of electromechanical characterization for a wide frequency range, presented in Sec. 4. Sec. 5 gives the results and discussion on the validation of the model and the effects of the design parameters on the actuator’s performance. Finally, the conclusions are drawn in Sec. 6.

2. Theoretical background and prior research

This section provides a brief theoretical background, necessary for the scientific part presented in Sec. 3. In Sec. 2.4, brief information about the recently presented, stacked actuator 3D-printed in a single process is given [41].

2.1. Dielectric electromechanical coupling

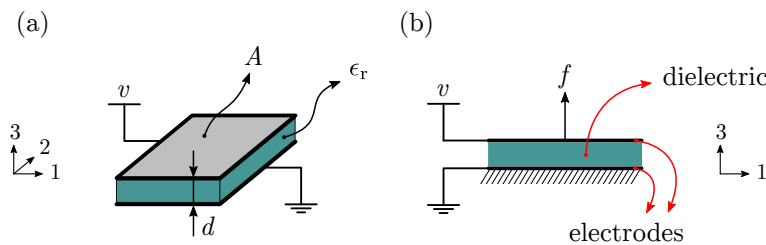


Figure 1: Simplified example of an active dielectric unit: (a) isometric view, (b) side view.

The theory of dielectric actuation mechanisms is based on a single active layer consisting of a dielectric film sandwiched between two opposing

electrodes, as shown in Fig.1. The dielectric actuation mechanism using the Maxwell-stress approach for the (33) direction is defined as [83]:

$$T_{33} = \frac{1}{2} \epsilon_r \epsilon_0 E_3^2. \quad (1)$$

The mechanical stress T_{33} generated in the dielectric layer is proportional to the relative permittivity ϵ_r (ϵ_0 is the permittivity of the vacuum) and the square of the electric field E_3 . The electric field:

$$E_3 = \frac{v}{d} \quad (2)$$

is established with a voltage potential v (applied to the opposing electrodes) and is inversely proportional to the thickness of the dielectric layer d , see Fig.1a.

If the electric field and mechanical stress are uniform, the generated force can be simplified to [84]:

$$f = -\frac{1}{2} \epsilon_r \epsilon_0 A \left(\frac{v}{d} \right)^2, \quad (3)$$

where A is the active area of the actuator, see Fig. 1a.

2.2. RC series circuit

In general, a dielectric actuator can be modeled electrically as an RC series circuit, where the resistor R represents the resistance of the electrodes, and the capacitor C represents the capacitance of the dielectric layer [84]. The electrical impedance $Z(\omega)$ of an RC series circuit, shown in Fig. 2a, is defined as:

$$Z(\omega) = \frac{V(\omega)}{I(\omega)} = R + \frac{1}{j\omega C}, \quad (4)$$

where $V(\omega)$ and $I(\omega)$ are the Fourier transform (FT) of the voltage applied to the electrodes and the current flowing through the circuit, respectively. An RC series circuit works like a low-pass filter with the cutoff frequency [84]:

$$f_{RC} = \frac{1}{2\pi RC}. \quad (5)$$

The cutoff frequency f_{RC} defines the frequency span of a dielectric actuator. The electrical transfer function used in this study, shown in Fig 2b, is defined

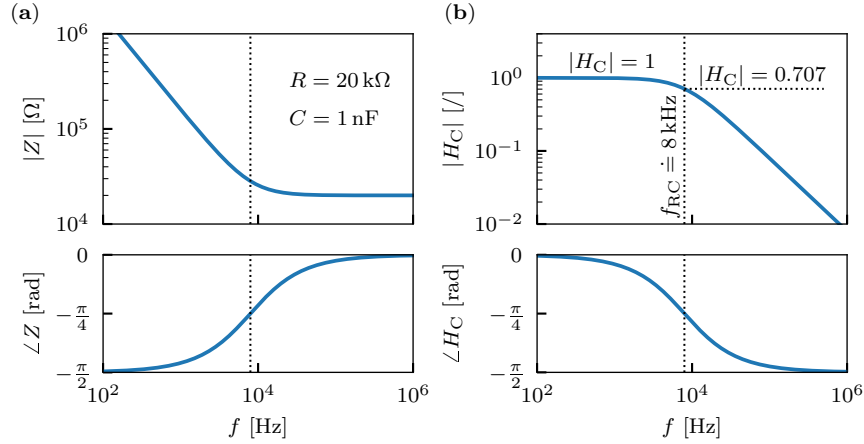


Figure 2: (a) Electrical impedance $Z(\omega)$ of a dielectric actuator. (b) Transfer function $H_C(\omega)$ of a dielectric actuator.

as:

$$H_C(\omega) = \frac{V_C(\omega)}{V(\omega)} = \frac{1}{1 + j\omega RC} = \frac{1}{j\omega C \cdot Z(\omega)}, \quad (6)$$

which converts the input voltage $V(\omega)$ to a voltage across the capacitor $V_C(\omega)$. From the transfer function $H_C(\omega)$ it is clear that the charge on the capacitor (dielectric layer) decreases drastically at $f > f_{RC}$, see $|H_C|(\omega)$ in Fig. 2b.

2.3. Dynamic frequency-dependent modulus

Thermoplastic elastomers have a pronounced frequency-dependent elasticity in the characterised frequency range (100 Hz to 5 kHz) [85], which must be included in the model. The elastic moduli for the materials used are defined using the frequency-dependent complex modulus [86]:

$$E^*(\omega) = E'(\omega) + jE''(\omega), \quad (7)$$

where E' is the real (storage) and E'' is the imaginary component (loss). The damping is defined by the loss tangent:

$$\tan \delta(\omega) = \frac{E''(\omega)}{E'(\omega)}. \quad (8)$$

2.4. Actuator design and fabrication

The design of a stacked dielectric actuator and the details of the 3D-printing process are described in detail in prior research [41]; only basic information is provided here.

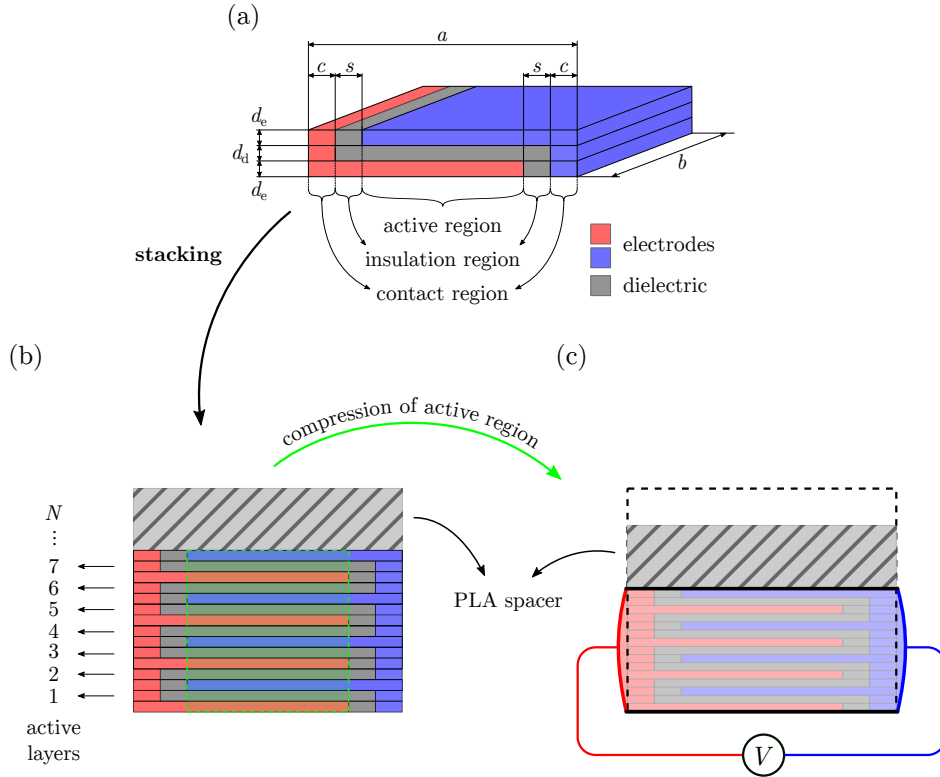


Figure 3: Design of the actuator: (a) the basic unit with two opposing electrodes with a dielectric between them, (b) a stacked actuator consisting of 7 active layers, with the active region highlighted in green, (c) the deformation of the stacked actuator during activation with a voltage potential at the opposing electrodes.

The design of the actuator is shown in Fig. 3. The base unit (Fig. 3a) consists of a dielectric sandwiched between two conductive layers. The active region is compressed when actuated, as shown in Fig. 3c. The insulating regions provide the necessary dielectric barrier between the opposing electrodes, and the contacting regions provide the conductive material at the edge of the actuator for an electrical connection (see Fig. 3a). A stacked actuator consists of N active layers (see Fig. 3b) The rigid spacer on top of the actuator serves as a mechanical connection for the experimental setups.

The design parameters that are the focus of this study are the active area A and the number of active layers N . The active area is obtained from the dimensions of the active unit:

$$A = (a - 2s - 2c) \cdot b, \quad (9)$$

where a , s , c and b represent the length of the active unit, the length of the insulation region, the length of the contact region and the width of the actuator, respectively (see Fig. 3a).

All the actuators were 3D printed using the E3D ToolChanger with four independent direct extruders, allowing the structures to be made from four different materials. The black TPU Flex filament (Plastika Trcek, Slovenia) was used for the dielectric areas and a conductive TPU composite from NinjaTek Eel (Fenner Inc., USA) was used for the conductive areas. The electrical contacts between the printed electrodes and the electrical excitation devices were fabricated manually using a conductive, embossed, tinned copper foil (3M, part number 1345) and conductive silver paint (ElectroLube, SCP), as described in prior research [41].

3. Electromechanical model

Solid-state dielectric actuators are operated with a high-voltage source. The voltage applied to the actuator's electrodes charges the dielectric regions of the actuator. The electromechanical coupling of the dielectric material (see theoretical background in Sec. 2.1) converts the electrical energy of the electric field into mechanical stress, which in turn deforms the dielectric. The electromechanical model must therefore take into account the (di)electrical properties of the conducting and dielectric materials, the electromechanical coupling of the dielectric, and the mechanical properties of the entire structure.

In this study, the model is conceptualised as shown in Fig. 4. The actuator is operated with an AC (sinusoidal) voltage without a DC bias. Since the dielectric effect is a nonlinear quadratic electromechanical coupling (1), the model is linearized by defining an input as a squared voltage. Therefore, V_{sq} represents the FT of the squared excitation voltage $v(t)$:

$$V_{\text{sq}}(\omega) = \mathcal{F} \{v^2(t)\}. \quad (10)$$

The electrical model $H_{\text{el}}(\omega)$ (Sec. 3.1) converts the voltage across the elec-

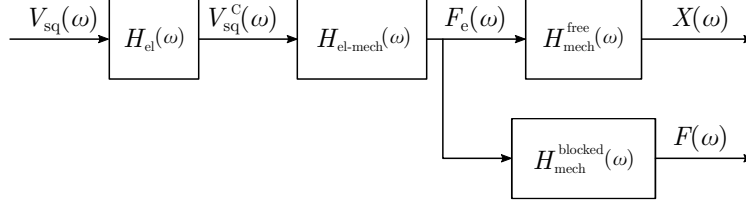


Figure 4: Electromechanical model that converts the squared input voltage $V_{\text{sq}}(\omega)$ applied to the contacts into the displacement $X(\omega)$ and force $F(\omega)$ of the stacked actuator.

trodes $V_{\text{sq}}(\omega)$ to the voltage across the capacitive elements $V_{\text{el}}^{\text{C}}(\omega)$ (dielectric layers):

$$V_{\text{sq}}^{\text{C}}(\omega) = H_{\text{el}}(\omega) \cdot V_{\text{sq}}(\omega). \quad (11)$$

The electromechanical coupling $H_{\text{el-mech}}(\omega)$ (Sec. 3.3) converts the voltage across the capacitive elements $V_{\text{sq}}^{\text{C}}(\omega)$ into the force $F_e(\omega)$ generated by the dielectric layers:

$$F_e(\omega) = H_{\text{el-mech}}(\omega) \cdot V_{\text{sq}}^{\text{C}}(\omega). \quad (12)$$

The force $F_e(\omega)$ is converted in the mechanical domain (Sec. 3.2) into a displacement of the actuator under the condition of free displacement:

$$X(\omega) = H_{\text{mech}}^{\text{free}}(\omega) \cdot F_e(\omega) \quad (13)$$

and into the force of the actuator under the condition of the blocked force:

$$F(\omega) = H_{\text{mech}}^{\text{blocked}}(\omega) \cdot F_e(\omega). \quad (14)$$

The actuator response to voltage excitation can be calculated for free-displacement operation as follows:

$$X(\omega) = H_{\text{mech}}^{\text{free}}(\omega) \cdot H_{\text{el-mech}}(\omega) \cdot H_{\text{el}}(\omega) \cdot V_{\text{sq}}(\omega) \quad (15)$$

and for the blocked force as:

$$F(\omega) = H_{\text{mech}}^{\text{blocked}}(\omega) \cdot H_{\text{el-mech}}(\omega) \cdot H_{\text{el}}(\omega) \cdot V_{\text{sq}}(\omega). \quad (16)$$

3.1. Electrical model

The lumped-electrical-elements model (resistors and capacitors) is shown in Fig. 5a. The resistance and capacitance are calculated from the dimensions and material properties (conductivity and permittivity), as shown in Fig. 5b.

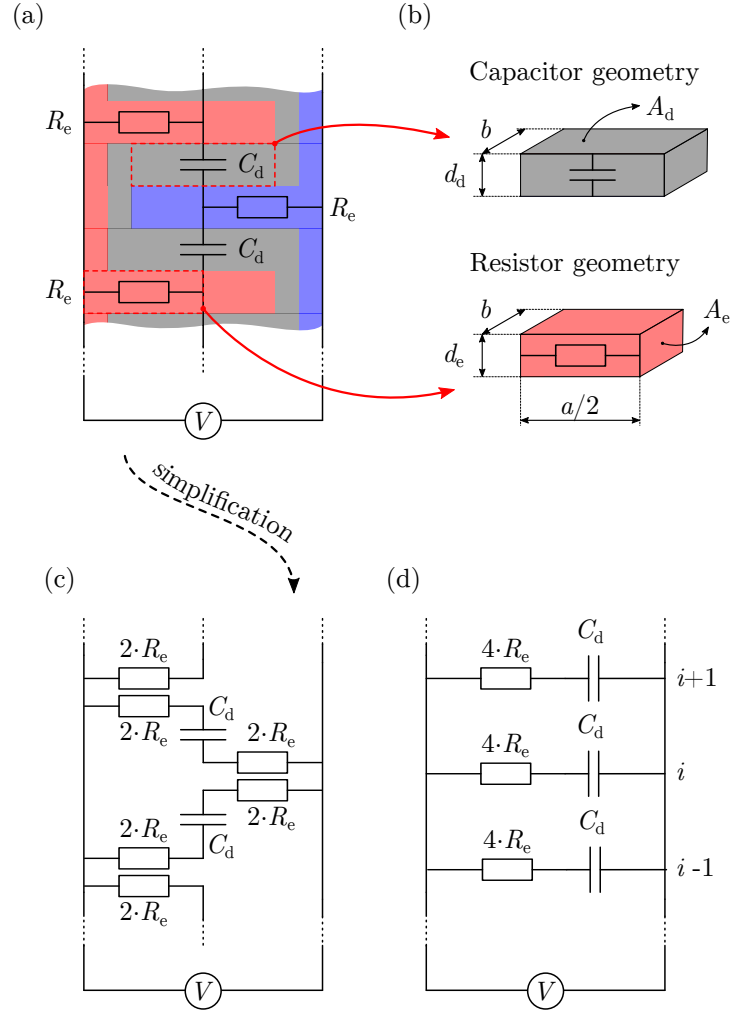


Figure 5: Electrical model of stacked actuator (not to scale). **(a)** Assembly of the resistors (electrodes) and capacitors (dielectric layers). **(b)** Definition of the geometry for the capacitance and resistance. **(c)** Simplification of the model to individual active layers. **(d)** Fully simplified model.

Fig. 5c and 5d show the reduction of the lumped-element model. The resistance R_e of each electrode is calculated from the electrode's geometry: length $a/2$ and cross-sectional area $A_e = b \cdot d_e$, using material conductivity σ , see Fig. 5b:

$$R_e = \frac{1}{\sigma} \frac{a/2}{A_e}. \quad (17)$$

The capacitance of a dielectric region C_d is defined as a capacitor with a relative permittivity ϵ_r , cross-sectional area $A_d = (a - 2(s + c)) \cdot b$ and the thickness d_d , see Fig. 5b:

$$C_d = \epsilon_r \epsilon_0 \frac{A_d}{d_d}, \quad (18)$$

where ϵ_0 is the permittivity of the vacuum. The charging of the insulation regions is negligible. The electrical impedance of the active layer is, see Fig. 5c:

$$Z_i(\omega) = 4R_e + \frac{1}{j\omega C_d}, \quad (19)$$

consisting of the resistance of the electrodes (17) and the capacitance of the dielectric (18). The electrical impedance of the actuator is equal to the N active layers connected in parallel (19):

$$Z(\omega) = \left(\sum_{i=1}^N \frac{1}{Z_i(\omega)} \right)^{-1}, \quad (20)$$

which is simplified to:

$$Z(\omega) = \left(N \frac{1}{Z_i(\omega)} \right)^{-1} = \frac{4j\omega R_e C_d + 1}{4Nj\omega R_e C_d} \quad (21)$$

The derived electrical impedance $Z(\omega)$ of the stacked actuator allows the calculation of the circuit transfer function $H_C(\omega)$, see Sec. 2.2 and Eq. (6):

$$H_C(\omega) = \frac{1}{j\omega C_\Sigma \cdot Z(\omega)}, \quad (22)$$

where C_Σ is the total capacitance of the stacked actuator:

$$C_\Sigma = N \cdot C_d. \quad (23)$$

The electrical model is defined by the electrical transfer function $H_C(\omega)$ (6):

$$H_{el}(\omega) = \frac{V_{sq}^C(\omega)}{V_{sq}(\omega)} = H_C^2 \left(\frac{\omega}{2} \right). \quad (24)$$

This calculation was validated using an experiment with a known RC series

circuit. The electrical cutoff frequency of the stacked actuator (5) is defined as:

$$f_{RC} = \frac{1}{2\pi R_{\Sigma} C_{\Sigma}}, \quad (25)$$

where R_{Σ} is the total resistance of the stacked actuator:

$$R_{\Sigma} = \frac{4R_e}{N}. \quad (26)$$

3.2. Dynamic model

The dynamic system with multiple degrees of freedom (MDOF) is modelled using lumped dynamic elements, see Fig. 6. The discrete DOFs are

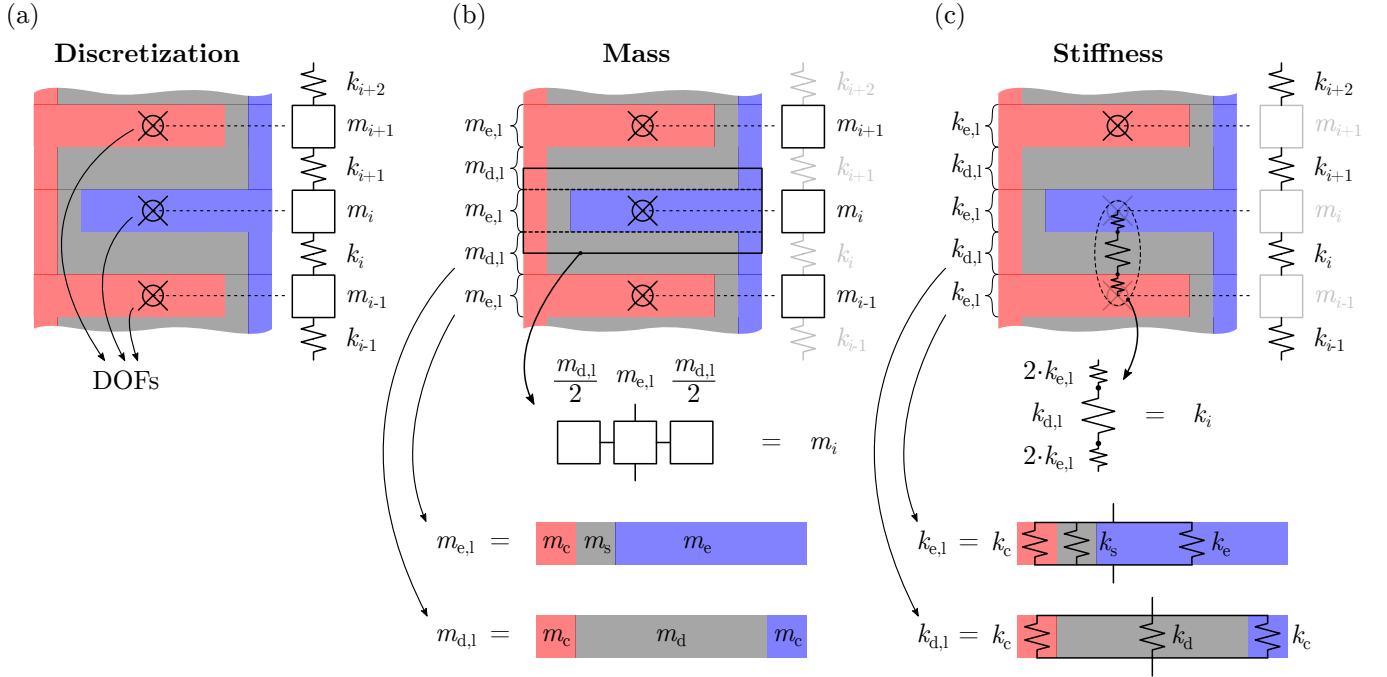


Figure 6: Dynamic model of a stacked dielectric actuator with lumped dynamic elements (a) discretization of a stacked dielectric actuator into individual DOFs located in the centre of the electrode layers, (b) definition of the mass of each individual DOF, (c) definition of the stiffness between the DOFs.

positioned in the centre of the electrode layers, see Fig. 6a.

Each discrete mass m_i corresponds to the mass of an electrode m_{el} and a

dielectric m_{dl} layer, see Fig. 6b:

$$m_i = m_{\text{el}} + m_{\text{dl}}, \quad (27)$$

The mass of the electrode layer includes the mass of the electrode m_e , the insulation m_s and the contact regions m_c :

$$m_{\text{el}} = m_e + m_s + m_c. \quad (28)$$

The mass of the dielectric layers is composed of two contact regions m_c and one dielectric region m_d :

$$m_{\text{dl}} = m_d + 2m_c. \quad (29)$$

The mass for each region was calculated with the known density of the conducting ρ_e and dielectric ρ_d materials, and the corresponding dimensions:

$$m_e = \rho_e \cdot (a - s - c) \cdot b \cdot d_e, \quad (30)$$

$$m_d = \rho_d \cdot (a - 2c) \cdot b \cdot d_d, \quad (31)$$

$$m_i = \rho_d \cdot s \cdot b \cdot d_e, \quad (32)$$

$$m_c = \rho_e \cdot c \cdot b \cdot d_e. \quad (33)$$

The stiffness of the connecting springs k_i is equal to the stiffness of the series-connected electrode k_{el} and the dielectric layers k_{dl} (see Fig. 6c):

$$k_i = \left(\frac{1}{k_{\text{el}}} + \frac{1}{k_{\text{dl}}} \right)^{-1}. \quad (34)$$

The stiffness of each layer corresponds to the stiffness of each region of the parallel connected layer. For the electrode layer:

$$k_{\text{el}} = k_c + k_s + k_e, \quad (35)$$

and the dielectric layer:

$$k_{\text{dl}} = k_d + 2k_c. \quad (36)$$

The stiffness of each region is calculated from the known elastic moduli of the conducting $E_e^*(\omega)$ and dielectric $E_d^*(\omega)$ materials and the corresponding

dimensions:

$$k_e = E_e^*(\omega) \cdot \frac{(a - s - c) \cdot b}{d_e}, \quad (37)$$

$$k_d = E_d^*(\omega) \cdot \frac{(a - 2c) \cdot b}{d_d}, \quad (38)$$

$$k_s = E_d^*(\omega) \cdot \frac{s \cdot b}{d_d}, \quad (39)$$

$$k_c = E_e^*(\omega) \cdot \frac{c \cdot b}{d_e}. \quad (40)$$

The differential equation of the dynamic MDOF system can be derived as:

$$\mathbf{M}\ddot{\mathbf{x}}(t) + \mathbf{K}^*(\omega)\mathbf{x}(t) = \mathbf{f}(t). \quad (41)$$

The matrices \mathbf{M} and $\mathbf{K}^*(\omega)$ are the mass matrix and the complex-frequency-dependent stiffness matrix, respectively; $\mathbf{x}(t)$ is the vector of vertical displacements of each DOF and $\mathbf{f}(t)$ is the vector of the external forces acting on each DOF.

3.3. Electromechanical coupling

The electromechanical coupling is based on Eq. (3). Here, the force $f(t)$ is proportional to the voltage $v_C(t)$, which represents the voltage potential across the capacitive elements of the actuator. For this reason, the generated force is defined as (3):

$$f(t) = f_{\text{coeff}} \cdot v_C^2(t), \quad (42)$$

where:

$$f_{\text{coeff}} = \frac{1}{2} \epsilon_r \epsilon_0 \frac{A}{d_d^2}. \quad (43)$$

The thickness of the dielectric d_d and the active area A are assumed to be constant during actuation because the measured strain of the stacked actuator is <1%.

The force is applied to each DOF of the dynamic model, as shown in Fig. 7. All the electrodes are pulled by a contracting dielectric region below and above the electrode, except for the top and bottom surfaces. Since the thicknesses d_d are assumed to be constant and an equal voltage is applied to all the electrodes (electrodes are connected in parallel), all the applied forces are equal. This means that the applied forces cancel out for all the

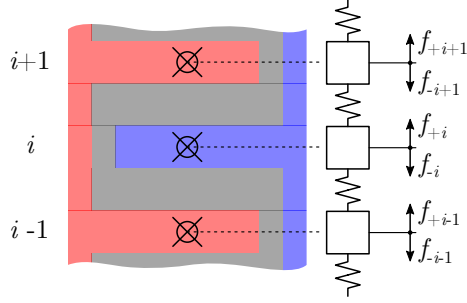


Figure 7: Application of the electromechanical coupling force to the dynamic model.

electrodes, except for the bottom and top electrodes. Therefore, the force vector $\mathbf{f}(t)$ contains only non-zero forces for the first and last DOF of the model:

$$\mathbf{f}(t) = \{+f_{\text{coeff}}, 0, \dots, 0, -f_{\text{coeff}}\}^T \cdot v_C^2(t). \quad (44)$$

The composed matrix differential equation (41) can now be transformed into the frequency domain using the FT. The FT of the force vector $\mathbf{f}(t)$ is obtained as follows:

$$\mathcal{F}\{\mathbf{f}(t)\} = \mathbf{f}_{\text{coeff}} \mathcal{F}\{v_C^2(t)\} = \mathbf{f}_{\text{coeff}} V_{\text{sq}}^C(\omega), \quad (45)$$

where $\mathbf{f}_{\text{coeff}}$ is a vector of the force coefficients in (44). The FT leads to an electro-mechanically coupled matrix equation in the frequency domain:

$$-\omega^2 \mathbf{M} \mathbf{X}(\omega) + \mathbf{K}^*(\omega) \mathbf{X}(\omega) = \mathbf{f}_{\text{coeff}} V_{\text{sq}}^C(\omega), \quad (46)$$

where $\mathbf{X}(\omega)$ is the FT of the vector of displacements $\mathbf{x}(t)$ and ω is the angular velocity. The transfer function between the displacements $\mathbf{X}(\omega)$ and the voltage across the dielectric layers $V_{\text{sq}}^C(\omega)$ is:

$$\frac{\mathbf{X}(\omega)}{V_{\text{sq}}^C(\omega)} = \frac{\mathbf{f}_{\text{coeff}}}{-\omega^2 \mathbf{M} + \mathbf{K}^*(\omega)}. \quad (47)$$

The electromechanical free-displacement characteristic of the actuator is defined as the displacement $X(\omega)$ divided by the driving voltage $V_{\text{sq}}(\omega)$. This can be calculated based on (47) and the definition of the electrical transfer

function $H_{\text{el}}(\omega)$ (11):

$$\mathbf{H}_{\text{x,v}}(\omega) = \frac{\mathbf{X}(\omega)}{V_{\text{sq}}(\omega)} = H_{\text{el}}(\omega) \cdot \frac{\mathbf{X}(\omega)}{V_{\text{sq}}^{\text{C}}(\omega)} = H_{\text{el}}(\omega) \cdot \frac{\mathbf{f}_{\text{coeff}}}{-\omega^2 \mathbf{M} + \mathbf{K}^*(\omega)}, \quad (48)$$

where $\mathbf{H}_{\text{x,v}}(\omega)$ is a vector of the frequency characteristics for each DOF. The DOF of interest in this study is the last DOF, representing the upper electrode.

The acceleration characteristic, defined as the acceleration $A(\omega)$ divided by the voltage $V_{\text{sq}}(\omega)$, was calculated from the displacement characteristic $\mathbf{H}_{\text{x,v}}(\omega)$:

$$\mathbf{A}(\omega) = -\omega^2 \mathbf{X}(\omega), \quad (49)$$

$$\mathbf{H}_{\text{a,v}}(\omega) = \frac{\mathbf{A}(\omega)}{V_{\text{sq}}(\omega)} = -\omega^2 \cdot \mathbf{H}_{\text{x,v}}(\omega). \quad (50)$$

For the blocked-force condition, the last DOF was excluded from the model ($x_n(t) = 0$). The reduced model is solved for the displacement characteristic $H_{\text{x,v}}(\omega)$, and the force characteristic is calculated as follows:

$$H_{\text{f,v}} = \frac{F(\omega)}{V_{\text{sq}}(\omega)} = H_{\text{x}_{n-1},\text{v}} \cdot k_n, \quad (51)$$

where $H_{\text{x}_{n-1},\text{v}}$ is the displacement characteristics of the $n - 1$ DOF (below the upper blocked DOF) and k_n is the stiffness between the n DOF (blocked) and $n - 1$ DOF (not blocked).

The main limitations of the proposed model arise from the linearization of the electromechanical coupling (10). The DC offset of the driving voltage and the change in thickness of the actuator during dynamic excitation (the thickness of the dielectric influences the generated force (3)) cannot be represented by the defined (linear) transfer functions. If these nonlinear effects are observed as non-negligible, the model can still be used by numerically integrating the coupled differential equation in the time domain. In this case, no linearization is required and the non-linear effects can be modelled.

4. Experimental research

Electrical characterization. The electrical properties of the materials used were measured on the printed samples using the method presented in Ap-

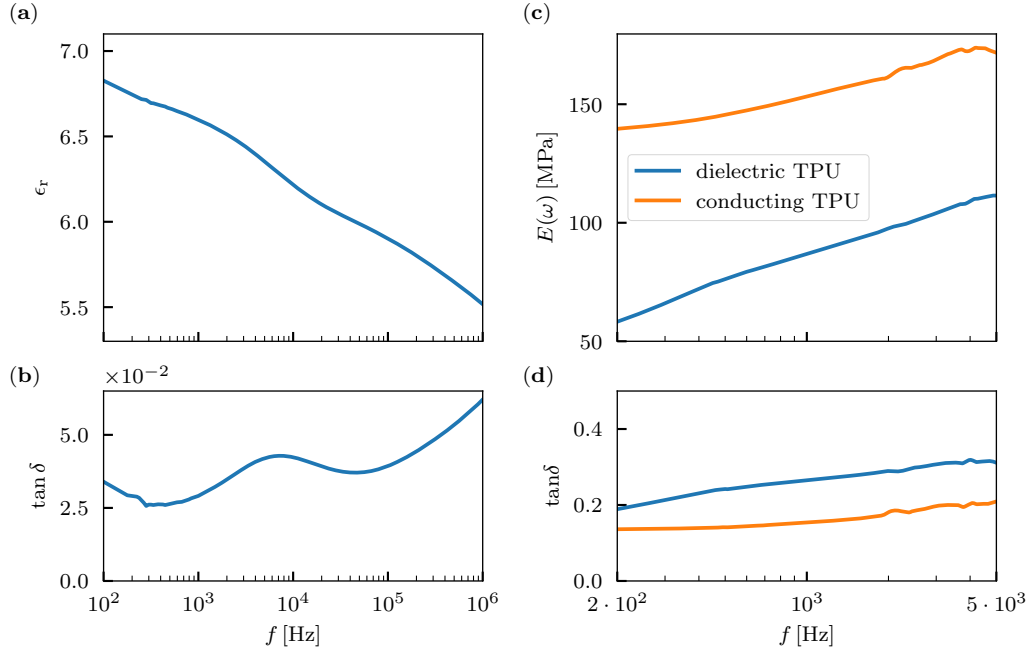


Figure 8: Electrical and mechanical properties of the materials used: (a) measured relative permittivity ϵ_r and (b) loss tangent $\tan \delta$ of the printed TPU used as the dielectric, (c) measured frequency-dependent elastic moduli of the conductive and dielectric TPUs, and (d) loss tangent of the TPUs.

pendix A. The measured permittivity of the dielectric is shown in Fig. 8a. The conductivity of the printed conductive TPU was measured to be 0.32 S/m.

Mechanical characterization. The frequency-dependent elastic moduli of the TPU materials were measured according to the method presented in Appendix B. The elastic properties for the dielectric and conductive TPUs are shown in Fig. 8c. The material densities were given by the manufacturer: dielectric TPU $\rho_d = 1.10 \text{ g/cm}^3$, conductive TPU $\rho_e = 1.18 \text{ g/cm}^3$ and PLA $\rho_{\text{PLA}} = 1.24 \text{ g/cm}^3$.

Electro-mechanical Characterization. The characterization methods for this research were adopted from previous research [41] with minor changes defined later in this section. Each 3D-printed actuator was experimentally characterised under a fixed-free and a fixed-fixed boundary condition, see Fig. 9.

For the free-displacement characterization, a PCB 352C33 piezoelectric

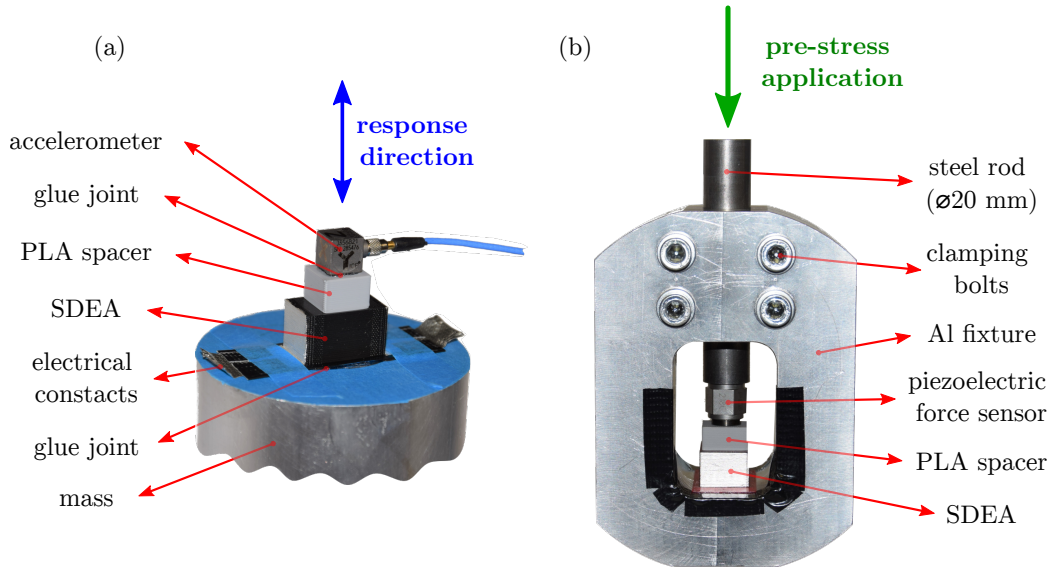


Figure 9: Experimental, dynamic electromechanical characterization of 3D-printed actuators [41]: (a) for free-displacement (fixed-free) boundary condition and (b) for blocked-force (fixed-fixed) boundary condition.

1-axis IEPE accelerometer (PCB Piezotronics, USA) was used to measure the vertical response (longitudinal contraction) of the free end of the actuator. The sensor signal was acquired using a NI9234 DAQ card and a NI cDAQ-9174 chassis.

The electromechanical free-displacement characteristic was defined as the acceleration $A(\omega)$ divided by the voltage $V_{sq}(\omega)$ (50):

$$H_{a,v}(\omega) = \frac{A(\omega)}{V_{sq}(\omega)} \left[\frac{\text{m/s}^2}{\text{V}^2} \right]. \quad (52)$$

For the characterization of the blocked force, the 3D-printed actuator was clamped in the fixture, as shown in Fig. 9b. Since the actuator contracts upon activation, the actuator must be preloaded to measure the actuation force and prevent the formation of a gap between the contacting surfaces. The preload force was applied by a threaded mechanism that pressed on the upper part of the steel rod (see Fig. 9b). During the application of the preload, the force was measured with a force sensor (PCB 218C) located between the steel rod and the actuator. Characterization was performed immediately

after the preload to minimize the viscoelastic effect of relaxation (reduction of the preload).

The static preload force and the dynamic actuation force were measured using a PCB 218C piezoelectric force sensor. The static charge (from the static preload force) was amplified with a Kistler 5073A charge amplifier. The dynamic charge (dynamic force) was amplified with a B&K Nexus 2692 charge amplifier. The voltage generated by the charge amplifiers was measured using a NI9232 DAQ card.

The fixed-fixed electromechanical characteristic was defined as the dynamic force $F(\omega)$ divided by the voltage $V_{sq}(\omega)$ (51):

$$H_{f,v}(\omega) = \frac{F(\omega)}{V_{sq}(\omega)} \left[\frac{\text{N}}{\text{V}^2} \right]. \quad (53)$$

5. Results and Discussion

For this study, 9 actuators with different active areas ($20 \times 20 \text{ mm}^2$, $15 \times 15 \text{ mm}^2$, $10 \times 10 \text{ mm}^2$) and number of layers (50, 100, 150) were 3D printed. The design parameters are shown in Tab. 1. Samples are denoted in the form N50-A20x20, where N50 represents 50 stacked layers and A20x20 represents a $20 \times 20 \text{ mm}^2$ (400 mm^2) active area.

Table 1: Design parameters for each actuator (dimensions according to Fig. 3): number of layers N , active area A , length a and width b .

N	50/100/150	50/100/150	50/100/150
$A \text{ [mm}^2\text{]}$	400	225	100
$a \text{ [mm]}$	24	19	14
$b \text{ [mm]}$	20	15	10

All the actuators were 3D printed with a layer thickness of 0.1 mm ($d_e = d_a = 0.1 \text{ mm}$), a contact area length of 1 mm ($c = 1 \text{ mm}$), and an isolation area length of 1.5 mm ($s = 1.5 \text{ mm}$), see Fig. 3.

5.1. Model validation

Here the results of the experimental electrical and electromechanical characterization are compared with the modeled electrical and electromechanical characteristics.

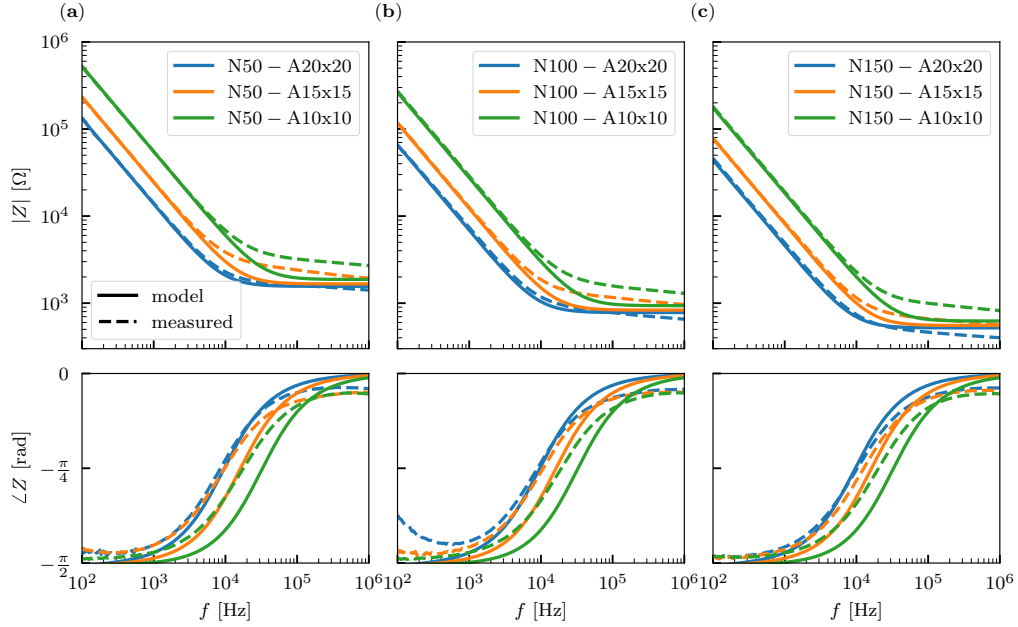


Figure 10: Measured and modeled electrical impedance Z for actuators with (a) 50 layers, (b) 100 layers, (c) 150 layers

Electrical impedance. The modeled electrical impedance (21) of the 3D-printed actuators is compared with the measured impedance in Fig. 10. The 3D-printed actuators show an electrical impedance typical for an RC series circuit. The cutoff frequency f_{RC} for the printed actuators is properly modeled and is in the range 10 to 35 kHz. A deviation from the measured impedance is seen in the resistive range (above the cutoff frequency), which is typical for distributed capacitive structures with high-resistance electrodes [87].

Free-displacement. Fig. 11 shows the dynamic free-displacement operation in terms of the acceleration characteristic (52). In free-displacement operation, the actuators exhibit resonant behavior. The model accurately predicts the resonant frequency and the magnitude of the acceleration characteristics below and above the resonance frequency. The model overestimates the magnitude of the response by approximately 5-10 %. The difference can be attributed to the stiff mechanical contacts on the bottom and top surfaces of the actuator [80, 79] and the insulating regions that store the electrical energy, but do not result in the vertical excitation force. The electrostatic

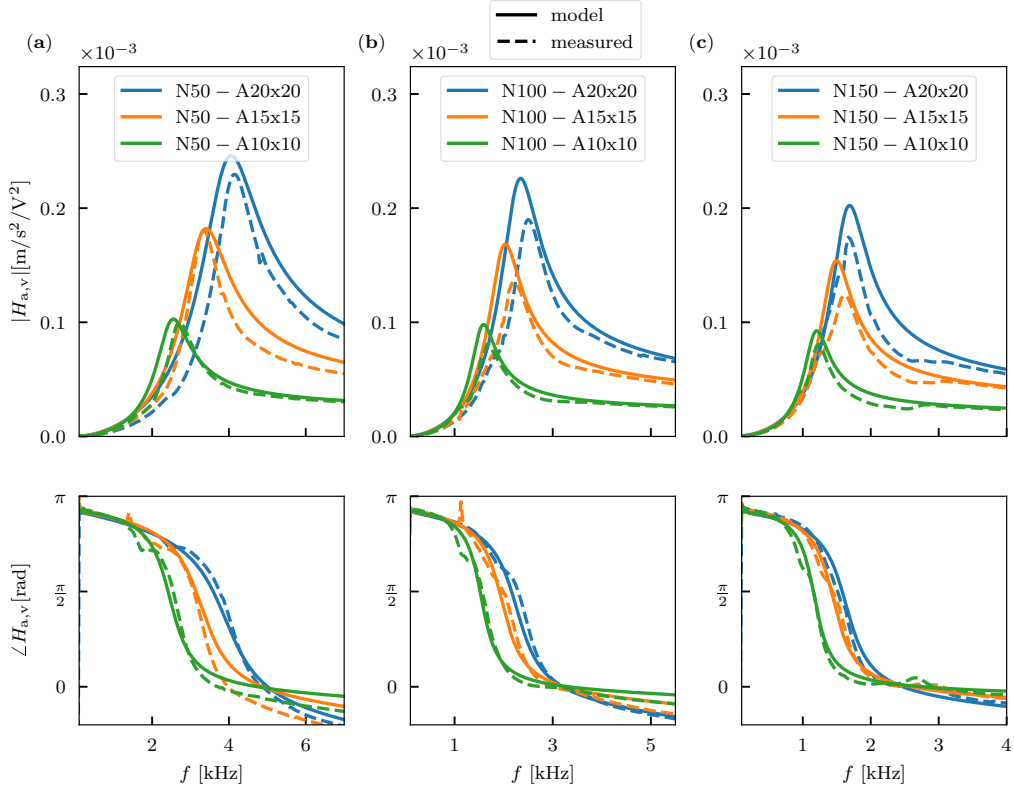


Figure 11: Dynamic free-displacement operation in the form of acceleration characteristics for the (a) 50-layer, (b) 100-layer, and (c) 150-layer actuators

finite-element analysis showed that the insulation regions in the actuator store 1-3% of the supplied electrical energy.

Blocked force. Fig. 12 shows the dynamic operation of each actuator under the blocked-force condition (53). The model shows a difference of approximately 20% compared to the experiment. Based on the experimental findings, the difference between the model and the measurements can be attributed to the effect of the static preload force, which is not included in the model. As discussed in Appendix C, the actuators have different stiffnesses, while the preload remains the same for all of them. Consequently, the pre-strain of each actuator layers is different, which affects the force generated by the compressed active layers (the layer thickness has a large effect on the force, see Eq. (3)) [88, 89].

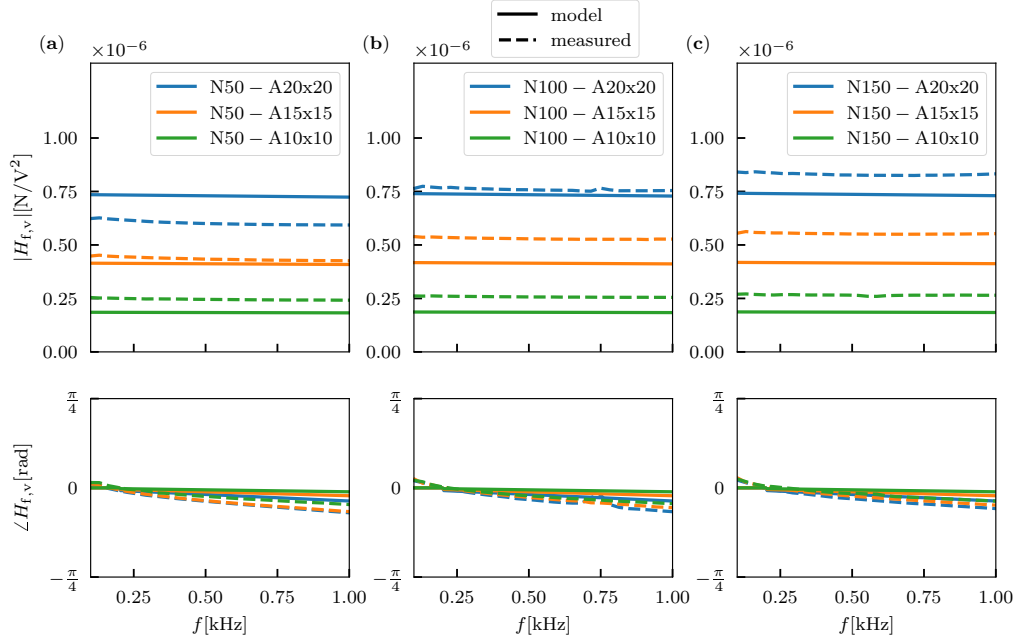


Figure 12: Dynamic blocked-force operation for: (a) 50-layer, (b) 100-layer, and (c) 150-layer actuators

5.2. Influence of design parameters on electromechanical response

The validated electromechanical model enables an investigation of the influence of the design parameters (active area A and number of active layers N) and the derivation of the design principles for the 3D-printed, dynamic, stacked dielectric actuators.

Electrical. In practise, the electrical cutoff frequency f_{RC} is the most important electrical property, since it limits the maximum operating frequency of a dielectric actuator. The effects of A and N on the cutoff frequency f_{RC} are plotted in Fig. 13.

Fig. 13a shows a step drop in the cutoff frequency f_{RC} with respect to the size of the active area A (25). This is due to the fact that the larger active area mainly increases the capacitance (18) and slightly decreases the resistance (17). To compensate for this effect, the resistance of the electrodes must be decreased, which can be achieved by increasing the conductive area of the electrodes by increasing the thickness of the electrode layers (17). The number of layers has no effect on the electrical cutoff frequency, since each

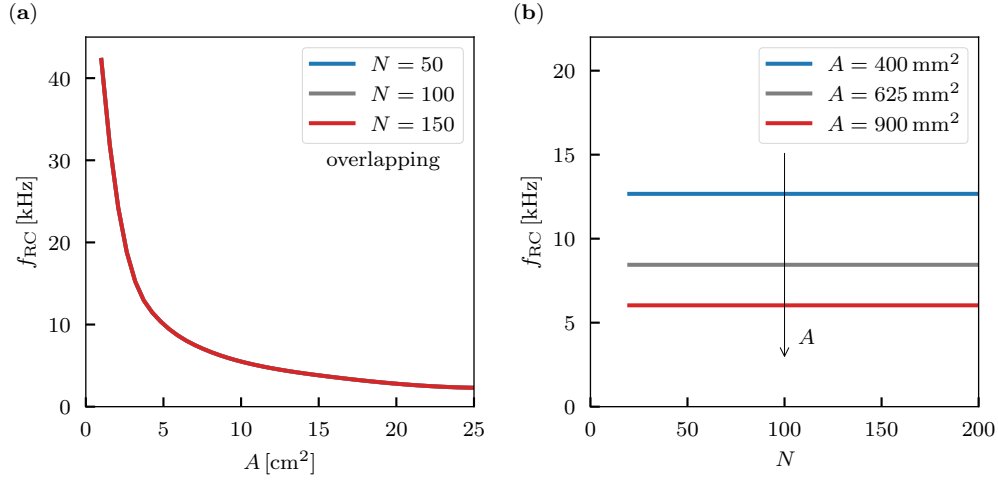


Figure 13: Effect of (a) active area A (model response is overlapping) and (b) number of stacked layers N on the electrical cutoff frequency f_{RC} of the actuators.

additional layer proportionally increases the capacitance (23) and decreases the total resistance of the actuator (26).

Electromechanical. The effect of the active area A on the electromechanical properties is shown in Fig. 14. The active area A affects the stiffness (37)-(40) and the mass (30)-(33) of each active unit (single dielectric layer) and the generated force (3) due to the electromechanical coupling.

The results in Fig. 14b show a clear, linear relationship between the blocked-force characteristic $H_{f,v}$ and the size of A . It is important to note that the deformation of the actuator is blocked and the change in the dynamic properties (stiffness and mass) does not affect the generated force. In the free-displacement condition the actuator responds with a dynamic displacement. Here, the effect of A is coupled by the effect on the generated force and the effect on the dynamic properties. Fig. 14a shows the effect of A on the resonance frequency f_{res} . The influencing factors here are the stiffness and the mass, both of which increase with increasing A . Depending on the number of layers N of the actuator and the active area A , a change in A will negligibly or drastically effect the resonance frequency f_{res} . A similar relationship can be observed between the acceleration characteristic $H_{a,v}$ and A in Fig. 14c. This figure represents the magnitude of the acceleration characteristic at resonance $H_{a,v}^{res}$ versus A , but the relationship can be observed

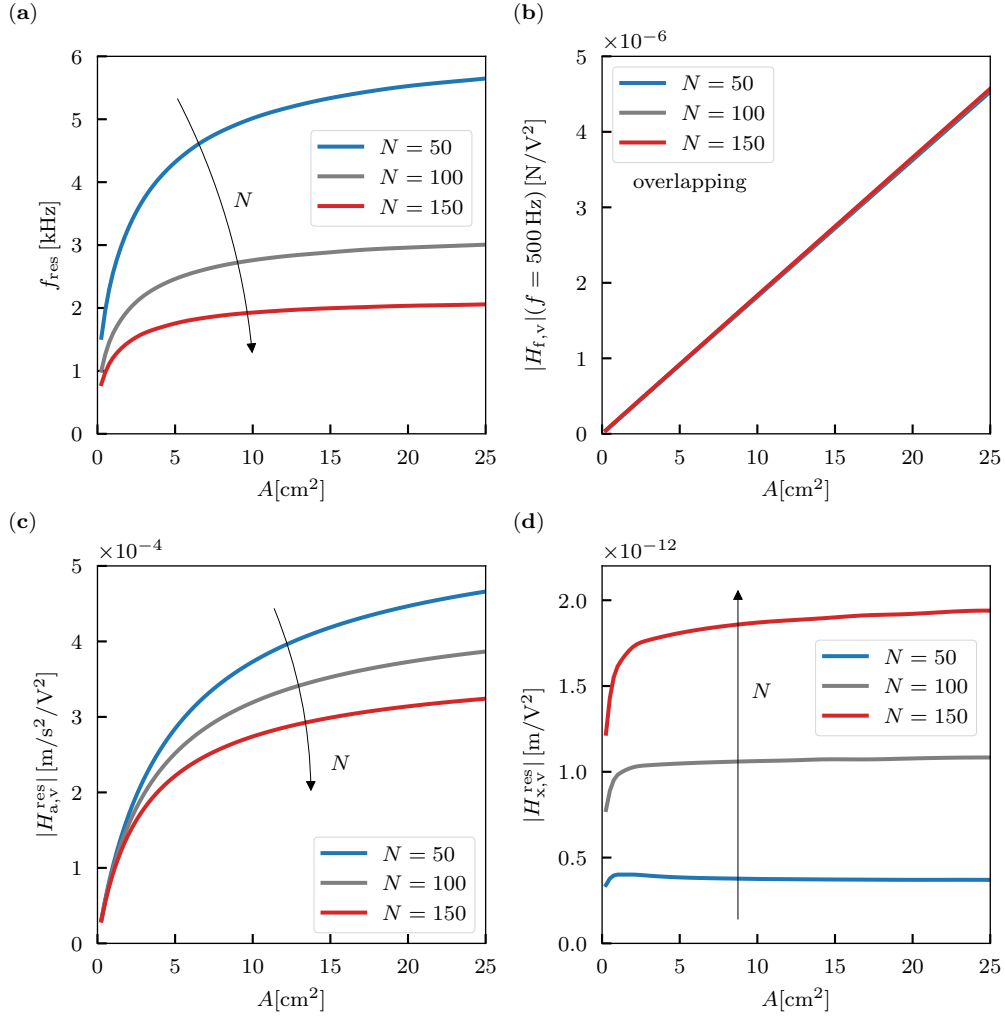


Figure 14: Effect of active area A on the electromechanical properties of an actuator: (a) the resonance frequency f_{res} , (b) the magnitude of the force characteristic at 500 Hz $H_{f,v}(f = 500\text{Hz})$, (c) the magnitude of the acceleration characteristic at resonance frequency $H_{a,v}^{\text{res}}$, (e) the magnitude of the displacement characteristic at resonance frequency $H_{x,v}^{\text{res}}$.

throughout the frequency response (see Fig. 11). Fig. 14d shows the effect of A on the displacement characteristics at resonance $H_{x,v}^{\text{res}}$. For the most part, increasing A does not increase the generated displacement. Although the generated force increases, the stiffness also increases and counteracts the

force, so that the change in the generated displacement is negligible. In the range of small A ($A < 2 \text{ cm}^2$), the effect of the passive area is observed. The contact and insulation regions (see Fig. 3) do not contribute to the generated force, but influence the response with the additional mass and stiffness. When the ratio of the active to passive area is low, the reducing effect of the passive regions becomes visible in the actuator's response.

The effect of the number of layers N on the electromechanical properties is shown in Fig. 15. The number of layers N , unlike A , does not affect the generated force, stiffness, or mass of the single active unit, but does affect the stiffness and mass of the entire stacked actuator. Each additional active layer adds mass and stiffness in series with the other layers. Adding stiffness in series reduces the stiffness of the entire stack. Although the additional active layers do not contribute to the generated force, they provide additional displacement of the entire stack.

The expected negligible effect on the generated force in a blocked condition is shown in Fig. 15b. Fig. 15a shows the effect of N on the resonance frequency f_{res} . The added mass and reduced stiffness with each additional active layer significantly reduce the f_{res} . Increasing N also decreases the magnitude of the acceleration characteristic $H_{a,v}$ as it reduces the resonance frequency f_{res} of the actuator, see Fig. 15c. The most significant effect of N can be seen in Fig. 15d, where increasing N significantly increases the displacement characteristic $H_{x,v}$. Added active layers reduce the stiffness of the whole stack and decrease the resonance frequency f_{res} . They also add the generated displacements of each added dielectric layer.

The presented analytical electromechanical model for 3D-printed stacked dielectric actuators provides a tool for predicting the performance of 3D-printed stacked dielectric actuators and guides the design process and optimization of parameters for specific applications. The results show that the active area has a significant effect on the electrical cutoff frequency (Fig. 13) and the generated force (Fig. 14), while the number of active layers has a significant effect on the achievable displacements of the actuator (Fig. 15). The findings on the relationship between the design parameters and the dynamic performance contribute to a deeper understanding of the electromechanical behavior of 3D-printed stacked dielectric actuators and provide information for the design and optimization of such actuators to achieve the desired dynamic properties.

The analytical model developed was validated under two specific boundary conditions (free-displacement and blocked-force). The model can be ex-

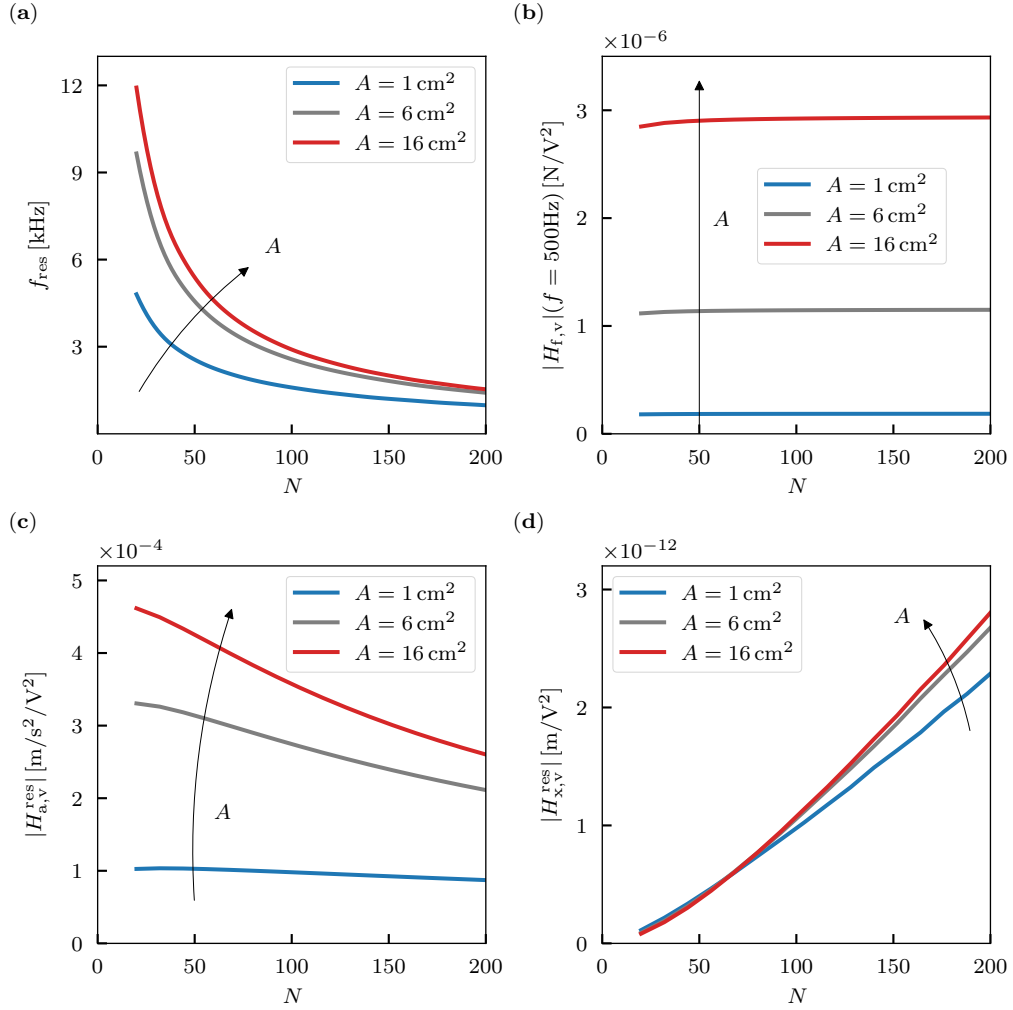


Figure 15: Effect of the number of layers N on the mechanical properties of an actuator: (a) the resonance frequency f_{res} , (b) the magnitude of the force characteristic at 500 Hz $H_{f,v}(f = 500\text{Hz})$, (c) the magnitude of the acceleration characteristic at resonance frequency $H_{a,v}^{\text{res}}$, (d) the magnitude of the displacement characteristic at resonance frequency $H_{x,v}^{\text{res}}$.

tended to other boundary conditions, e.g stacked actuators embedded in a smart structure.

6. Conclusions

In the design phase of an individualised 3D-printed actuator, it is important to consider all the design parameters (A , N , layer thickness d_e and d_d) and the affected electromechanical properties (resonance f_{res} , force $H_{f,v}$, acceleration $H_{s,v}$, and displacement $H_{x,v}$). The parameters have a coupled effect on the properties, so several parameters must be adjusted to achieve the desired property.

The electromechanical model introduced in this research is based on the design parameters of a 3D-printed, stacked dielectric actuator and the material properties of the commercial thermoplastic elastomers. The model was validated on nine 3D-printed behaviours with different design parameters. The standard dynamic elements and a clear model structure allow a reliable prediction of the dynamic characteristics of a 3D-printed actuator over a wide frequency range.

The influence of the active area and the number of stacked layers was investigated to derive the main design principles of 3D-printed stacked actuators for different application areas. It was shown that the properties, *i.e.*, the electrical cutoff frequency f_{RC} , the resonance frequency f_{res} , the magnitude of the free displacement and the magnitude of the blocked force, can be tailored to the desired application and size constraints.

The resonance f_{res} of an actuator can be tuned to the desired frequency with the active area A and/or the number of layers N . This is particularly useful for resonator applications where a specific resonance is required. The generated force can be directly modulated with the size of the active area A . This is useful in situations where the actuator is blocked or must actuate large (stiff, heavy) loads, such as vibration-isolation applications. The generated displacement can be modulated most effectively with the number of layers N , which is suitable for individualised, 3D-printed, nanopositioning systems.

Acknowledgements

The authors acknowledge the partial financial support from the Slovenian Research Agency (research core funding No. P2-0263 and research project J2-3045).

Appendix A. Electrical characterization of 3D-printed conductive and dielectric TPUs

The resistivity of the conductive TPU used for 3D-printed electrodes was measured directly using the method presented in [14].

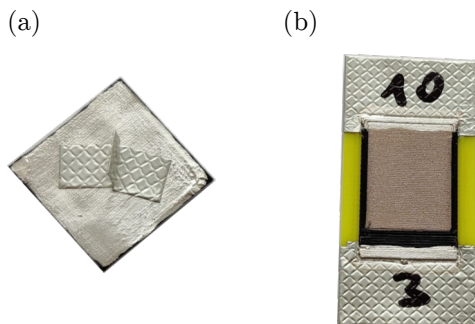


Figure A.16: samples for permittivity measurement: (a) with manually attached electrodes, (b) with printed electrodes.

The relative permittivity of the dielectric TPU was measured on the 3D-printed samples. Both the 3D-printed and manually applied electrodes were tested. The samples are shown in Fig. A.16. Conductive Electrify filament (Multi3D, USA) and NinjaTek Eel conductive TPU (used for the actuators) were tested for the printed electrodes. Conductive silver paint (ElectroLube, SCP) was used for the manual application of the electrodes. The tested electrode materials had no significant effect on the capacitance measurement, i.e., none of the conductive materials contributed significantly to the capacitance. However, if the capacitance must be measured at high frequencies, the electrodes must be sufficiently conductive not to lower the electrical cutoff frequency below the desired measurement range.

The measurement was performed using two-probe impedance method on a Digilent Analog Discovery 2 oscilloscope (Digilent Inc., USA) with an impedance measurement module. The module allowed impedance measurements with calibrated shunt resistors and compensation for the connecting cables.

The series capacitance of the dielectric layer C can be calculated from the measured reactance $X(\omega)$ directly:

$$C(\omega) = -\frac{1}{\omega X}. \quad (\text{A.1})$$

For the best results, the frequency range of the calculation should be well below the cutoff frequency. The frequency-dependent relative permittivity ϵ_r is calculated from the capacitance and the known dimensions of the dielectric layer:

$$\epsilon_r(\omega) = C(\omega) \frac{d}{A \epsilon_0}, \quad (\text{A.2})$$

where A and d are the area and thickness of the dielectric layer, respectively, and ϵ_0 is the permittivity of the vacuum.

This method provides a straight-forward approach to the electrical characterization of 3D-printed structures composed of dielectric and conductive materials.

Appendix B. Mechanical characterization of 3D-printed TPU

The modulus of elasticity was determined by experimentally characterising the mechanical impedance $Z(\omega)$ of the 3D-printed TPU samples. For each material (NinjaTek Eel and Trcel Flex TPU), a cylindrical sample with a thickness of 0.4 mm (2 layers) and a diameter of 12 mm was 3D printed. The samples were positioned in the test fixture shown in Fig. B.17. The samples were dynamically excited by a preloaded piezo actuator (P-212.10 PICA, Physik Instrumente, Germany) and the applied dynamic force and acceleration were measured with an impedance sensor (PCB 288D01, PCB Piezotronics, USA).

The mechanical impedance $Z(\omega)$ was calculated from the measured force $F(\omega)$ and acceleration $A(\omega)$:

$$Z(\omega) = \frac{F(\omega)}{V(\omega)}, \quad (\text{B.1})$$

where the velocity $V(\omega)$ was calculated from the acceleration $A(\omega)$:

$$V(\omega) = \frac{A(\omega)}{j\omega}. \quad (\text{B.2})$$

To calculate the stiffness of the sample, the effect of the mass was calculated:

$$Z_m(\omega) = j\omega m, \quad (\text{B.3})$$

where m is the sum of the oscillating masses composed of the sensor endplate

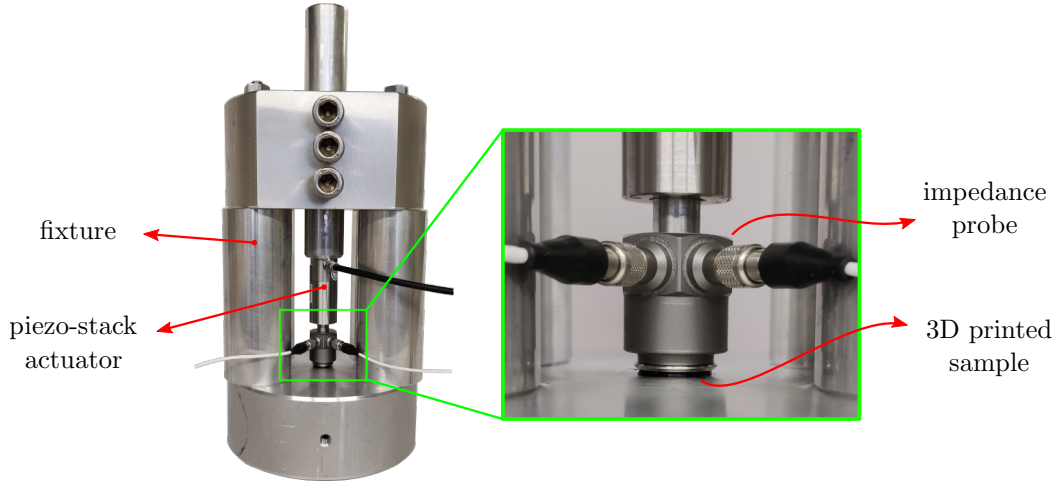


Figure B.17: Experimental setup for measuring the mechanical impedance of 3D-printed TPU samples.

and the sample. The stiffness impedance $Z_k(\omega)$ was calculated by subtracting the mass impedance $Z(\omega)$ from the measured impedance $Z(\omega)$:

$$Z_k(\omega) = Z(\omega) - Z_m(\omega). \quad (\text{B.4})$$

From the stiffness $k^*(\omega)$:

$$k^*(\omega) = j\omega Z_k(\omega) \quad (\text{B.5})$$

the complex frequency-dependent modulus $E^*(\omega)$ was calculated:

$$E^*(\omega) = k^*(\omega) \frac{d}{S}, \quad (\text{B.6})$$

where d is the thickness of the sample and S is the cross-sectional area.

Theoretically, the stiffness can be estimated for the entire excitation-frequency range, including resonance frequencies. However, experiments have shown that the results below the first resonance of the test setup are the most reliable. In this case, the first resonance of the setup consisting of the fixture, piezoelectric actuator and impedance probe was around 8 kHz. When the sample was fixed in the test setup, the first resonance decreased to about 6 kHz. For this reason, the most reliable results were obtained below 5 kHz.

Appendix C. The effect of mechanical preload on the blocked force

The mechanical preload of the stacked dielectric actuator is required for measuring the force characteristics (see Sec. 4). The static preload force has a significant effect on the measured dynamic force generated by the actuator. Fig. C.18 shows the force characteristics of an N50-A20x20 actuator with 0.15 mm layer thickness characterized at three different preload forces. The

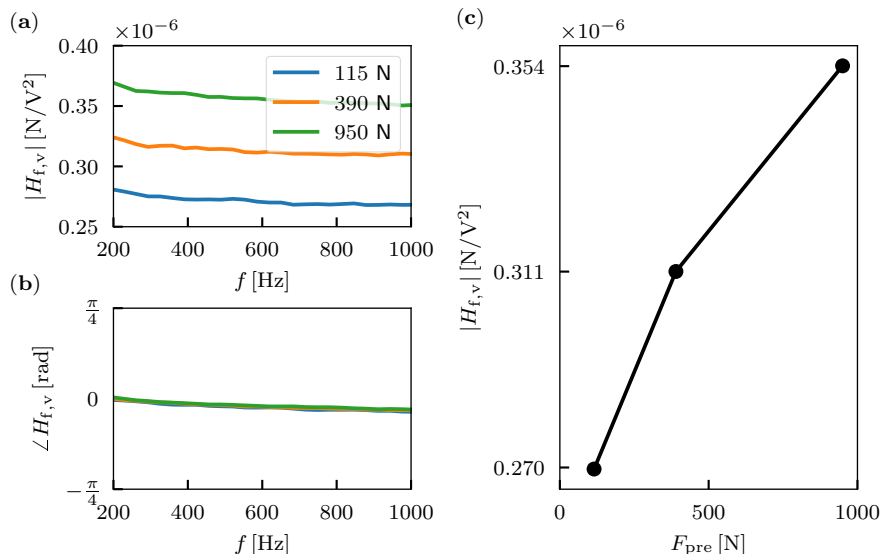


Figure C.18: (a) Magnitude of force characteristics $H_{f,v}(\omega)$ for three different preload forces. (b) Phase of the force characteristic. (c) Mean magnitude of $H_{f,v}(\omega)$ as a function of preload force.

generated force increases with the applied static preload force, increasing by 31 % from 115 N to 950 N. The preload force compresses the active layers (decreases the thickness), which increases the electric field in the dielectric and thus increases the generated force.

References

- [1] A. Georgopoulou, L. Egloff, B. Vanderborght, F. Clemens, A Soft Pneumatic Actuator with Integrated Deformation Sensing Elements Produced Exclusively with Extrusion Based Additive Manufacturing, in: The 8th International Symposium on Sensor Science, MDPI, Basel Switzerland, 2021, p. 11. doi:10.3390/I3S2021Dresden-10097.

- [2] T. Hainsworth, L. Smith, S. Alexander, R. MacCurdy, A Fabrication Free, 3D Printed, Multi-Material, Self-Sensing Soft Actuator, *IEEE Robotics and Automation Letters* 5 (3) (2020) 4118–4125. doi:10.1109/LRA.2020.2986760.
- [3] K. R. Ryan, M. P. Down, C. E. Banks, Future of additive manufacturing: Overview of 4D and 3D printed smart and advanced materials and their applications, *Chemical Engineering Journal* 403 (2021) 126162. doi:10.1016/j.cej.2020.126162.
- [4] J. Lee, H. C. Kim, J. W. Choi, I. H. Lee, A review on 3D printed smart devices for 4D printing, *International Journal of Precision Engineering and Manufacturing - Green Technology* 4 (3) (2017) 373–383. doi:10.1007/s40684-017-0042-x.
- [5] T. Košir, J. Slavič, Modeling of Single-Process 3D-Printed Piezoelectric Sensors with Resistive Electrodes: The Low-Pass Filtering Effect, *Polymers* 15 (1) (2022) 158. doi:10.3390/polym15010158.
- [6] M. Arh, J. Slavič, M. Boltežar, Design principles for a single-process 3d-printed accelerometer – theory and experiment, *Mechanical Systems and Signal Processing* 152 (2021) 107475. doi:10.1016/j.ymssp.2020.107475.
- [7] M. Arh, J. Slavič, Single-Process 3D-Printed Triaxial Accelerometer, *Advanced Materials Technologies* (2021) 2101321doi:10.1002/admt.202101321.
- [8] T. Košir, J. Slavič, Single-process fused filament fabrication 3D-printed high-sensitivity dynamic piezoelectric sensor, *Additive Manufacturing* 49 (2022) 102482. doi:10.1016/j.addma.2021.102482.
- [9] H. Watschke, M. Goutier, J. Heubach, T. Vietor, K. Leichsenring, M. Böhl, Novel Resistive Sensor Design Utilizing the Geometric Freedom of Additive Manufacturing, *Applied Sciences* 11 (1) (2020) 113. doi:10.3390/app11010113.
- [10] Q. Yi, S. Najafikhoshnoo, P. Das, S. Noh, E. Hoang, T. Kim, R. Esfandyarpour, All-3D-Printed, Flexible, and Hybrid Wearable Bioelectronic Tactile Sensors Using Biocompatible Nanocomposites for Health

- Monitoring, *Advanced Materials Technologies* 7 (5) (2022) 2101034. doi:10.1002/admt.202101034.
- [11] M. O. F. Emon, F. Alkadi, D. G. Philip, D. H. Kim, K. C. Lee, J. W. Choi, Multi-material 3D printing of a soft pressure sensor, *Additive Manufacturing* 28 (2019) 629–638. doi:10.1016/j.addma.2019.06.001.
- [12] H. Liu, H. Zhang, W. Han, H. Lin, R. Li, J. Zhu, W. Huang, 3D Printed Flexible Strain Sensors: From Printing to Devices and Signals, *Advanced Materials* 33 (8) (2021) 2004782. doi:10.1002/adma.202004782.
- [13] M. Maurizi, J. Slavič, F. Cianetti, M. Jerman, J. Valentinčič, A. Lebar, M. Boltežar, Dynamic measurements using FDM 3D-printed embedded strain sensors, *Sensors (Switzerland)* 19 (12) (2019). doi:10.3390/s19122661.
- [14] T. B. Palmić, J. Slavič, M. Boltežar, Process parameters for 3d-printed conductors for applications in sensors, *Sensors (Switzerland)* 20 (16) (2020) 1–21. doi:10.3390/s20164542.
- [15] Z. Lei, Z. Chen, Y. Zhou, Y. Liu, J. Xu, D. Wang, Y. Shen, W. Feng, Z. Zhang, H. Chen, Novel electrically conductive composite filaments based on Ag/saturated polyester/polyvinyl butyral for 3D-printing circuits, *Composites Science and Technology* 180 (2019) 44–50. doi:10.1016/J.COMPSCITECH.2019.05.003.
- [16] P. F. Flowers, C. Reyes, S. Ye, M. J. Kim, B. J. Wiley, 3D printing electronic components and circuits with conductive thermoplastic filament, *Additive Manufacturing* 18 (2017) 156–163. doi:10.1016/j.addma.2017.10.002.
- [17] Z. Lyu, G. J. Lim, J. J. Koh, Y. Li, Y. Ma, J. Ding, J. Wang, Z. Hu, J. Wang, W. Chen, Y. Chen, Design and Manufacture of 3D-Printed Batteries, *Joule* 5 (1) (2021) 89–114. doi:10.1016/j.joule.2020.11.010.
- [18] C. Reyes, R. Somogyi, S. Niu, M. A. Cruz, F. Yang, M. J. Catenacci, C. P. Rhodes, B. J. Wiley, Three-Dimensional Printing of a Complete Lithium Ion Battery with Fused Filament Fabrication, *ACS Applied Energy Materials* 1 (10) (2018) 5268–5279. doi:10.1021/acsaem.8b00885.

- [19] M. Mallick, L. Franke, A. G. Rösch, U. Lemmer, Shape-Versatile 3D Thermoelectric Generators by Additive Manufacturing, *ACS Energy Letters* 6 (1) (2021) 85–91. doi:10.1021/acsenergylett.0c02159.
- [20] D. Ni, R. Heisser, B. Davaji, L. Ivy, R. Shepherd, A. Lal, Polymer interdigitated pillar electrostatic (PIPE) actuators, *Microsystems & Nanoengineering* 8 (1) (2022) 18. doi:10.1038/s41378-021-00328-0.
- [21] M. Osada, G. Zhang, F. Carneiro, M. Muromachi, S. Yoshimoto, A. Yamamoto, Effect of insulating liquid viscosity on output force of a high-power synchronous electrostatic motor, *International Journal of Mechanical Sciences* 220 (2022) 107149. doi:10.1016/j.ijmecsci.2022.107149.
- [22] Y. Huang, J. Chen, M. Zhao, M. Feng, Electromechanical coupling characteristics of double-layer piezoelectric quasicrystal actuators, *International Journal of Mechanical Sciences* 196 (2021) 106293. doi:10.1016/j.ijmecsci.2021.106293.
- [23] R. S. Reddy, S. Panda, A. Gupta, Nonlinear dynamics and active control of smart beams using shear/extensional mode piezoelectric actuators, *International Journal of Mechanical Sciences* 204 (2021) 106495. doi:10.1016/j.ijmecsci.2021.106495.
- [24] A. D. Charles, A. N. Rider, S. A. Brown, C. H. Wang, Multifunctional magneto-polymer matrix composites for electromagnetic interference suppression, sensors and actuators, *Progress in Materials Science* 115 (2021) 100705. doi:10.1016/j.pmatsci.2020.100705.
- [25] Y. Jang, H. Nabae, G. Endo, K. Suzumori, Analysis of the multi-balloon dielectric elastomer actuator for traveling wave motion, *Sensors and Actuators A: Physical* 333 (2022) 113243. doi:10.1016/j.sna.2021.113243.
- [26] P. Kumar, B. Muralidharan, D. N. Pawaskar, M. M. Inamdar, Investigation of phonon lasing like auto-parametric instability between 1-D flexural modes of electrostatically actuated microbeams, *International Journal of Mechanical Sciences* 220 (2022) 107135. doi:10.1016/j.ijmecsci.2022.107135.

- [27] T. Hiruta, N. Hosoya, S. Maeda, I. Kajiwara, Experimental validation of vibration control in membrane structures using dielectric elastomer actuators in a vacuum environment, *International Journal of Mechanical Sciences* 191 (2021) 106049. doi:10.1016/j.ijmecsci.2020.106049.
- [28] E. Garnell, C. Rouby, O. Doaré, Dynamics and sound radiation of a dielectric elastomer membrane, *Journal of Sound and Vibration* 459 (2019) 114836. doi:10.1016/J.JSV.2019.07.002.
- [29] L. Medina, A. A. Seshia, Tristable properties and limit point behaviour in electrostatically actuated initially curved coupled micro beams, *International Journal of Mechanical Sciences* 204 (2021) 106543. doi:10.1016/j.ijmecsci.2021.106543.
- [30] B. Sparrman, C. du Pasquier, C. Thomsen, S. Darbari, R. Rustom, J. Laucks, K. Shea, S. Tibbits, Printed silicone pneumatic actuators for soft robotics, *Additive Manufacturing* 40 (2021) 101860. doi:10.1016/J.ADDMA.2021.101860.
- [31] T. Hanuhov, N. Cohen, Thermally induced deformations in multi-layered polymeric struts, *International Journal of Mechanical Sciences* 215 (2022) 106959. doi:10.1016/j.ijmecsci.2021.106959.
- [32] O. Ulkir, Design and fabrication of an electrothermal MEMS micro-actuator with 3D printing technology, *Materials Research Express* 7 (7) (2020) 075015. doi:10.1088/2053-1591/aba8e3.
- [33] F. Long, Y. Cheng, Y. Ren, J. Wang, Z. Li, A. Sun, G. Xu, Latest Advances in Development of Smart Phase Change Material for Soft Actuators, *Advanced Engineering Materials* 24 (3) (2022) 2100863. doi:10.1002/adem.202100863.
- [34] Z. Zhao, K. Wang, L. Zhang, L.-C. Wang, W.-L. Song, D. Fang, Stiff reconfigurable polygons for smart connectors and deployable structures, *International Journal of Mechanical Sciences* 161-162 (2019) 105052. doi:10.1016/j.ijmecsci.2019.105052.
- [35] A. M. Soomro, F. H. Memon, J.-W. Lee, F. Ahmed, K. H. Kim, Y. S. Kim, K. H. Choi, Fully 3D printed multi-material soft bio-inspired frog

- for underwater synchronous swimming, *International Journal of Mechanical Sciences* 210 (2021) 106725. doi:10.1016/j.ijmecsci.2021.106725.
- [36] G. Zhong, W. Dou, X. Zhang, H. Yi, Bending analysis and contact force modeling of soft pneumatic actuators with pleated structures, *International Journal of Mechanical Sciences* 193 (2021) 106150. doi:10.1016/j.ijmecsci.2020.106150.
- [37] W. Xiao, X. Du, W. Chen, G. Yang, D. Hu, X. Han, Cooperative collapse of helical structure enables the actuation of twisting pneumatic artificial muscle, *International Journal of Mechanical Sciences* 201 (2021) 106483. doi:10.1016/j.ijmecsci.2021.106483.
- [38] L. M. Fonseca, G. V. Rodrigues, M. A. Savi, An overview of the mechanical description of origami-inspired systems and structures, *International Journal of Mechanical Sciences* 223 (2022) 107316. doi:10.1016/j.ijmecsci.2022.107316.
- [39] X. Cao, S. Xuan, Y. Gao, C. Lou, H. Deng, X. Gong, 3D Printing Ultraflexible Magnetic Actuators via Screw Extrusion Method, *Advanced Science* 9 (16) (2022) 2200898. doi:10.1002/advs.202200898.
- [40] H. Tiismus, A. Kallaste, T. Vaimann, A. Rassõlkin, State of the art of additively manufactured electromagnetic materials for topology optimized electrical machines, *Additive Manufacturing* 55 (2022) 102778. doi:10.1016/j.addma.2022.102778.
- [41] T. B. Palmić, J. Slavič, Single-process 3D-printed stacked dielectric actuator, *International Journal of Mechanical Sciences* 230 (2022) 107555. doi:10.1016/j.ijmecsci.2022.107555.
- [42] A. Chortos, E. Hajiesmaili, J. Morales, D. R. Clarke, J. A. Lewis, 3D Printing of Interdigitated Dielectric Elastomer Actuators, *Advanced Functional Materials* 30 (1) (2020) 1907375. doi:10.1002/adfm.201907375.
- [43] I. Kierzewski, S. S. Bedair, B. Hanrahan, H. Tsang, L. Hu, N. Lazarus, Adding an electroactive response to 3D printed materials: Printing a piezoelectret, *Additive Manufacturing* 31 (2020) 100963. doi:10.1016/J.ADDMA.2019.100963.

- [44] Y. Zhang, N. Zhang, H. Hingorani, N. Ding, D. Wang, C. Yuan, B. Zhang, G. Gu, Q. Ge, Fast-Response, Stiffness-Tunable Soft Actuator by Hybrid Multimaterial 3D Printing, *Advanced Functional Materials* 29 (15) (2019) 1806698. doi:10.1002/adfm.201806698.
- [45] X. Wei, H. Li, X. He, Z. Li, H. Ye, W. Xue, Q. Ge, Shape Memory Polymer-based Stiffness Variable Soft Actuator Via Digital Light Processing-based 3D Printing, in: 2021 27th International Conference on Mechatronics and Machine Vision in Practice (M2VIP), IEEE, 2021, pp. 612–616. doi:10.1109/M2VIP49856.2021.9665032.
- [46] J. Shintake, D. Ichige, R. Kanno, T. Nagai, K. Shimizu, Monolithic Stacked Dielectric Elastomer Actuators, *Frontiers in Robotics and AI* 8 (2021). doi:10.3389/frobt.2021.714332.
- [47] G. Haghiashtiani, E. Habtour, S.-H. Park, F. Gardea, M. C. McAlpine, 3D printed electrically-driven soft actuators, *Extreme Mechanics Letters* 21 (2018) 1–8. doi:10.1016/j.eml.2018.02.002.
- [48] M. Tyagi, G. M. Spinks, E. W. H. Jager, Fully 3D printed soft microactuators for soft microrobotics, *Smart Materials and Structures* 29 (8) (2020) 085032. doi:10.1088/1361-665X/ab9f48.
- [49] H. M. Wang, Viscoelastic analysis of a spring-connected dielectric elastomer actuator undergoing large inhomogeneous deformation, *International Journal of Mechanical Sciences* 136 (2018) 17–23. doi:10.1016/j.ijmecsci.2017.12.004.
- [50] H. Zhao, A. M. Hussain, M. Duduta, D. M. Vogt, R. J. Wood, D. R. Clarke, Compact Dielectric Elastomer Linear Actuators, *Advanced Functional Materials* 28 (42) (2018). doi:10.1002/ADFM.201804328.
- [51] M. R. O’Neill, E. Acome, S. Bakarich, S. K. Mitchell, J. Timko, C. Keplinger, R. F. Shepherd, Rapid 3D Printing of Electrohydraulic (HASEL) Tentacle Actuators, *Advanced Functional Materials* 30 (40) (2020) 2005244. doi:10.1002/adfm.202005244.
- [52] K. Yu, A. Xin, H. Du, Y. Li, Q. Wang, Additive manufacturing of self-healing elastomers, *NPG Asia Materials* 2019 11:1 11 (1) (2019) 1–11. doi:10.1038/s41427-019-0109-y.

- [53] W. Sun, H. Liang, F. Zhang, H. Wang, Y. Lu, B. Li, G. Chen, Dielectric elastomer minimum energy structure with a unidirectional actuation for a soft crawling robot: design, modeling, and kinematic study, *International Journal of Mechanical Sciences* (2022) 107837.
- [54] Q. He, Z. Wang, Y. Wang, A. Minori, M. T. Tolley, S. Cai, Electrically controlled liquid crystal elastomer-based soft tubular actuator with multimodal actuation, *Science Advances* 5 (10) (oct 2019). doi:10.1126/SCIADV.AAX5746.
- [55] M. Duduta, E. Hajiesmaili, H. Zhao, R. J. Wood, D. R. Clarke, Realizing the potential of dielectric elastomer artificial muscles, *Proceedings of the National Academy of Sciences of the United States of America* 116 (7) (2019) 2476–2481. doi:10.1073/pnas.1815053116.
- [56] X. Ji, X. Liu, V. Cacucciolo, M. Imboden, Y. Civet, A. E. Haitami, S. Cantin, Y. Perriard, H. Shea, An autonomous untethered fast soft robotic insect driven by low-voltage dielectric elastomer actuators, *Science Robotics* 4 (37) (dec 2019). doi:10.1126/SCIROBOTICS.AAZ6451.
- [57] C. Christianson, C. Bayag, G. Li, S. Jadhav, A. Giri, C. Agba, T. Li, M. T. Tolley, Jellyfish-Inspired Soft Robot Driven by Fluid Electrode Dielectric Organic Robotic Actuators, *Frontiers in Robotics and AI* 6 (2019). doi:10.3389/frobt.2019.00126.
- [58] R. Chen, Z. Yuan, J. Guo, L. Bai, X. Zhu, F. Liu, H. Pu, L. Xin, Y. Peng, J. Luo, L. Wen, Y. Sun, Legless soft robots capable of rapid, continuous, and steered jumping, *Nature Communications* 12 (1) (2021) 7028. doi:10.1038/s41467-021-27265-w.
- [59] M. Duduta, F. C. Berlinger, R. Nagpal, D. R. Clarke, R. J. Wood, F. Z. Temel, Electrically-latched compliant jumping mechanism based on a dielectric elastomer actuator, *Smart Materials and Structures* 28 (9) (2019). doi:10.1088/1361-665X/AB3537.
- [60] Y. Chen, H. Zhao, J. Mao, P. Chirarattananon, E. F. Helbling, N. s. P. Hyun, D. R. Clarke, R. J. Wood, Controlled flight of a microrobot powered by soft artificial muscles, *Nature* 575 (7782) (2019) 324–329. doi:10.1038/s41586-019-1737-7.

- [61] M. Ghilardi, H. Boys, P. Török, J. J. C. Busfield, F. Carpi, Smart Lenses with Electrically Tuneable Astigmatism, *Scientific Reports* 2019 9:1 9 (1) (2019) 1–10. doi:10.1038/s41598-019-52168-8.
- [62] C. R. Kelley, J. L. Kauffman, Towards wearable tremor suppression using dielectric elastomer stack actuators, *Smart Materials and Structures* 30 (2) (2021) 025006. doi:10.1088/1361-665X/abccdc.
- [63] A. Bruschi, D. M. Donati, P. Choong, E. Lucarelli, G. Wallace, Dielectric Elastomer Actuators, Neuromuscular Interfaces, and Foreign Body Response in Artificial Neuromuscular Prostheses: A Review of the Literature for an In Vivo Application, *Advanced Healthcare Materials* 10 (13) (2021) 2100041. doi:10.1002/adhm.202100041.
- [64] X. Ji, X. Liu, V. Cacucciolo, Y. Civet, A. El Haitami, S. Cantin, Y. Perriard, H. Shea, Untethered Feel-Through Haptics Using 18- μm Thick Dielectric Elastomer Actuators, *Advanced Functional Materials* (2020) 2006639doi:10.1002/adfm.202006639.
- [65] S. Hau, G. Rizzello, M. Hodgins, A. York, S. Seelecke, Design and control of a high-speed positioning system based on dielectric elastomer membrane actuators, *IEEE/ASME Transactions on Mechatronics* 22 (3) (2017) 1259–1267. doi:10.1109/TMECH.2017.2681839.
- [66] I. Kajiwara, S. Kitabatake, N. Hosoya, S. Maeda, Design of dielectric elastomer actuators for vibration control at high frequencies, *International Journal of Mechanical Sciences* 157-158 (2019) 849–857. doi:10.1016/j.ijmecsci.2019.05.019.
- [67] T. Lu, C. Ma, T. Wang, Mechanics of dielectric elastomer structures: A review, *Extreme Mechanics Letters* 38 (2020) 100752. doi:10.1016/j.eml.2020.100752.
- [68] D. L. Henann, S. A. Chester, K. Bertoldi, Modeling of dielectric elastomers: Design of actuators and energy harvesting devices, *Journal of the Mechanics and Physics of Solids* 61 (10) (2013) 2047–2066. doi:10.1016/j.jmps.2013.05.003.
- [69] A. K. Sharma, M. M. Joglekar, A numerical framework for modeling anisotropic dielectric elastomers, *Computer Methods in Applied Me-*

- chanics and Engineering 344 (2019) 402–420. doi:10.1016/J.CMA.2018.10.005.
- [70] K. Jia, M. Wang, T. Lu, T. Wang, Linear control of multi-electrode dielectric elastomer actuator with a finite element model, *International Journal of Mechanical Sciences* 159 (2019) 441–449. doi:10.1016/j.ijmecsci.2019.06.015.
- [71] H. Li, L. Chen, C. Zhao, S. Yang, Evoking or suppressing electromechanical instabilities in soft dielectrics with deformation-dependent dielectric permittivity, *International Journal of Mechanical Sciences* 202-203 (2021) 106507. doi:10.1016/j.ijmecsci.2021.106507.
- [72] W. C. Zinan Zhao, Yingjie Chen, Xueyan Hu, Ronghao Bao, Bin Wu, Vibrations and waves in soft dielectric elastomer structures, *International Journal of Mechanical Sciences* (2022) 107885doi:https://doi.org/10.1016/j.ijmecsci.2022.107885.
- [73] Y. Chen, B. Wu, Y. Su, W. Chen, Effects of strain stiffening and electrostriction on tunable elastic waves in compressible dielectric elastomer laminates, *International Journal of Mechanical Sciences* 176 (2020) 105572. doi:10.1016/j.ijmecsci.2020.105572.
- [74] J. Zhu, H. Chen, B. Wu, W. Chen, O. Balogun, Tunable band gaps and transmission behavior of SH waves with oblique incident angle in periodic dielectric elastomer laminates, *International Journal of Mechanical Sciences* 146-147 (2018) 81–90. doi:10.1016/j.ijmecsci.2018.07.038.
- [75] J. Zhang, L. Tang, L. Liu, J. Zhao, Z. Yang, P. Li, Modeling of humidity effect on electromechanical properties of viscoelastic dielectric elastomer, *International Journal of Mechanical Sciences* 193 (2021) 106177. doi:10.1016/j.ijmecsci.2020.106177.
- [76] T. Karner, J. Gotlih, Viscoelastic constitutive models and their fractional representatives to capture the time-dependent response of DEAs on sinus excitation, *Smart Materials and Structures* 30 (8) (2021). doi:10.1088/1361-665X/ac1305.

- [77] L. He, J. Lou, J. Du, J. Wang, Finite bending of a dielectric elastomer actuator and pre-stretch effects, *International Journal of Mechanical Sciences* 122 (2017) 120–128. doi:10.1016/j.ijmecsci.2017.01.019.
- [78] Z. Wang, B. He, Y. Zhou, R. Shen, G. Li, Effects of pre-stretch on the oscillation and stability of dielectric elastomers, *International Journal of Mechanical Sciences* 185 (2020) 105879. doi:10.1016/j.ijmecsci.2020.105879.
- [79] G. Kovacs, L. Düring, S. Michel, G. Terrasi, Stacked dielectric elastomer actuator for tensile force transmission, *Sensors and Actuators, A: Physical* 155 (2) (2009) 299–307. doi:10.1016/j.sna.2009.08.027.
- [80] S. Kuhring, D. Uhlenbusch, T. Hoffstadt, J. Maas, Finite element analysis of multilayer DEAP stack-actuators, in: *Electroactive Polymer Actuators and Devices (EAPAD) 2015*, Vol. 9430, SPIE, 2015, p. 94301L. doi:10.1117/12.2085121.
- [81] H. Haus, M. Matysek, H. Mößinger, H. F. Schlaak, Modelling and characterization of dielectric elastomer stack actuators, *Smart Materials and Structures* 22 (10) (2013) 104009. doi:10.1088/0964-1726/22/10/104009.
- [82] T. Hoffstadt, J. Maas, Analytical modeling and optimization of DEAP-based multilayer stack-transducers, *Smart Materials and Structures* 24 (9) (2015) 094001. doi:10.1088/0964-1726/24/9/094001.
- [83] R. Pelrine, R. Kornbluh, Q. Pei, J. Joseph, High-speed electrically actuated elastomers with strain greater than 100%, *Science* 287 (5454) (2000) 836–839. doi:10.1126/science.287.5454.836.
- [84] F. Carpi, I. Anderson, S. Bauer, G. Frediani, G. Gallone, M. Gei, C. Graaf, C. Jean-Mistral, W. Kaal, G. Kofod, M. Kollosche, R. Kornbluh, B. Lassen, M. Matysek, S. Michel, S. Nowak, B. O’Brien, Q. Pei, R. Pelrine, B. Rechenbach, S. Rosset, H. Shea, Standards for dielectric elastomer transducers, *Smart Materials and Structures* 24 (10) (2015) 105025. doi:10.1088/0964-1726/24/10/105025.
- [85] M. Aurilia, F. Piscitelli, L. Sorrentino, M. Lavorgna, S. Iannace, Detailed analysis of dynamic mechanical properties of TPU nanocomposite: The

- role of the interfaces, *European Polymer Journal* 47 (5) (2011) 925–936. doi:10.1016/j.eurpolymj.2011.01.005.
- [86] A. Helal, M. Doumit, R. Shaheen, Biaxial experimental and analytical characterization of a dielectric elastomer, *Applied Physics A* 124 (1) (2018) 2. doi:10.1007/s00339-017-1422-3.
- [87] F. Rafik, H. Gualous, R. Gallay, A. Crausaz, A. Berthon, Frequency, thermal and voltage supercapacitor characterization and modeling, *Journal of Power Sources* 165 (2) (2007) 928–934. doi:10.1016/j.jpowsour.2006.12.021.
- [88] B. Li, H. Chen, J. Qiang, S. Hu, Z. Zhu, Y. Wang, Effect of mechanical pre-stretch on the stabilization of dielectric elastomer actuation, *Journal of Physics D: Applied Physics* 44 (15) (2011) 155301. doi:10.1088/0022-3727/44/15/155301.
- [89] G. Kofod, The static actuation of dielectric elastomer actuators: How does pre-stretch improve actuation?, *Journal of Physics D: Applied Physics* 41 (21) (2008) 215405. doi:10.1088/0022-3727/41/21/215405.